THESIS FOR THE DEGREE OF LICENCIATE OF ENGINEERING

Optical characterisation of subwavelength dielectric particles using particle tracking beyond the Stokes-Einstein relation

ERIK OLSÉN

CHALMERS
UNIVERSITY OF TECHNOLOGY

Department of Physics
CHALMERS UNIVERSITY OF TECHNOLOGY
Gothenburg, Sweden 2021

Optical characterisation of subwavelength dielectric particles using particle tracking beyond the Stokes-Einstein relation

ERIK OLSÉN

Department of Physics
Chalmers University of Technology
SE-412 96 Gothenburg
Sweden
Telephone + 46 (0)31-772 1000

Chalmers Digitaltryck
Gothenburg, Sweden 2021

Cover illustration: Schematic example of Brownian motion for a particle in a microfluidic channel under fluid flow. From the optical illumination (green shaded region) and quantification of the subsequent optical signal as the particle moves in the channel, different particle properties can be quantified, such as refractive index, size, slip length and changes in the particle signal.

Optical characterisation of subwavelength dielectric particles using particle tracking beyond the Stokes-Einstein relation

Erik Olsén
Department of Physics
Chalmers University of Technology
SE-412 96 Gothenburg
Sweden

Abstract

As the importance of nanoparticles continues to increase in both biology and industrial processes, so does the need for accurate and versatile characterization methods. However, most light-based methods to quantify size and refractive index of individual particles are either limited to snapshot observations, particles larger than the wavelength of light, non-dynamic particle properties, and commonly, the hydrodynamic boundary conditions are assumed without experimental evaluation of the assumptions. The aim of this thesis is to partially overcome these limitations by further developing two different characterisation methods based on optical microscopy combined with particle tracking, where in both cases, the analysis goes beyond the ordinary Stokes-Einstein relation.

The first method combines off-axis holographic nanoparticle tracking with deep learning (Paper I). By utilizing the optical signal, both size and refractive index of individual particles with a minimum size of $R = 150$ nm were accurately determined using only five particle observations. The method was evaluated using particles of different sizes, refractive indices, surrounding media as well as for nanoparticle clusters, for which reversible fluctuations of the number of monomers could be resolved for polystyrene nanoparticle clusters, while the fractal dimension remained constant.

The second method is based around tethering particles to a fluid lipid bilayer and quantifying their diffusivity and flow-induced motion (Paper II). By separating the friction contributions from the tethers and the particle, simultaneous measurement of size and diffusivity enabled a comparison with theory using partial slip as a fitting parameter. This was used to quantify the slip length for different lipid vesicles, as well as clarifying the size-dependent mechanistic aspects concerning the mobility of membrane-attached nanoparticles.

Keywords: Optical microscopy, off-axis holography, particle tracking, size determination, particle dynamics, lipid vesicles, partial slip

Those swirls in the cream mixing into the coffee? That's us.
Ephemeral patterns of complexity, riding a wave of increasing entropy from simple beginnings to a simple end.
We should enjoy the ride.

- Sean Carroll

List of publications

The papers appended in this thesis are listed below. The papers are referred to using their roman numerals throughout the thesis.

Paper I:

Fast and Accurate Nanoparticle Characterization Using Deep-Learning-Enhanced Off-Axis Holography

Benjamin Midtvedt, Erik Olsén. Fredrik Eklund, Fredrik Höök, Caroline Beck Adiels, Giovanni Volpe, and Daniel Midtvedt

ACS Nano 2021, 15, 2, 2240–2250

My contribution: I was responsible for the design and planning of the experiments. I built the experimental setup, performed the experiments and participated significantly in the data analysis as well as the writing of the article.

Paper II:

Quantification of Diffusion for Lipid Vesicles Attached to a Supported Lipid Bilayer Suggests the Partial-Slip Boundary Condition

Erik Olsén[*], Silver Jõemetsa[*], Adrián González Rodríguez, Paul Joyce, Vladimir P. Zhdanov, Daniel Midtvedt, and Fredrik Höök

Submitted

My contribution: I was responsible for the idea behind the investigation and most of planning of the experiments. I performed the majority of the data analysis and wrote the manuscript.

[*] Shared first-author

Publications not included in the thesis

Evaluation of Pressure Generated by Resistors From Different Positive Expiratory Pressure Devices
Monika Fagevik Olsén, Maria Carlsson, Erik Olsén, and Elisabeth Westerdahl
Respiratory care 2015, 60 (10) 1418-1423

Multidimensional hybridization of dark surface plasmons
Andrew B. Yankovich, Ruggero Verre, Erik Olsén, Anton E. O. Persson, Viet Trinh, Gudrun Dovner, Mikael Käll, and Eva Olsson
ACS Nano 2017, 11, 4, 4265–4274

Label-free spatio-temporal monitoring of cytosolic mass, osmolarity, and volume in living cells
Daniel Midtvedt, Erik Olsén, Fredrik Höök, and Gavin D. M. Jeffries
Nat Commun 2019, 10, 340

Visualizing spatial variations of plasmon-exciton polaritons at the nanoscale using electron microscopy
Andrew B. Yankovich, Battulga Munkhbat, Denis G. Baranov, Jorge Cuadra, Erik Olsén, Hugo Lourenço-Martins, Luiz H. G. Tizei, Mathieu Kociak, Eva Olsson, and Timur Shegai
Nano Lett. 2019, 19, 11, 8171–8181

Size and Refractive Index Determination of Subwavelength Particles and Air Bubbles by Holographic Nanoparticle Tracking Analysis
Daniel Midtvedt, Fredrik Eklund, Erik Olsén, Benjamin Midtvedt, Jan Swenson, and Fredrik Höök
Anal. Chem. 2020, 92, 2, 1908–1915

Constructing a library of metal and metal–oxide nanoparticle heterodimers through colloidal assembly
Tina A. Gschneidtner, Sarah Lerch, Erik Olsén, Xin Wen, Amelia C. Y. Liu, Alicja Stolaś, Joanne Etheridge, Eva Olsson and Kasper Moth-Poulsen
Nanoscale 2020,12, 11297-11305

FRET-Based Assay for the Quantification of Extracellular Vesicles and Other Vesicles of Complex Composition
Konrad Thorsteinsson, Erik Olsén, Eneas Schmidt, Hudson Pace, and Marta Bally
Anal. Chem. 2020, 92, 23, 15336–15343

Contents

1 Introduction 1
2 Optical imaging theory 5
2.1 Huygens–Fresnel principle of wave propagation 7
2.2 Propagation of angular spectrum 9
2.3 Optical resolution limit 10
2.4 Optical signal from small particles 11
2.5 Fluorescence 13
3 Brownian motion 15
3.1 Hydrodynamic boundary conditions 18
3.2 Confined particle diffusion 19
3.3 Brownian motion of nanoparticles tethered to a lipid bilayer 21
3.4 Estimation of diffusion constant from particle tracking 21
4 Experimental methods 23
4.1 Quantitative phase microscopy 23
4.1.1 Optical off-axis holographic microscopy 26
4.1.2 Characterisation of subwavelength particles using their optical signal 27
4.1.3 Image analysis of holography data using deep learning 29
4.2 Two-dimensional flow nanometry 30
4.2.1 Limitations of two-dimensional flow nanometry 32
4.2.2 Total internal reflection fluorescence microscopy 33
4.3 Comparison between optical holography and different microscopy characterisation techniques to estimate particle size 35
5 Summary of results 37
5.1 Paper I 37
5.2 Paper II 40
6 Future outlook 43
6.1 Off-axis twilight holography 43
6.2 Holographic characterisation of sub-cellular structures using deep learning 46
6.3 Diffusivity quantification of tethered particles with surface interaction 48
Acknowledgements 49
References 50

List of abbreviations and definitions

Textual abbreviations

2DFN	Two-dimensional flow nanometry
CNN	Convolutional neural networks
COBRI	Coherent brightfield microscopy
EVs	Extracellular vesicles
FRAP	Fluorescence recovery after photobleaching
H-NTA	Off-axis holographic nanoparticle tracking analysis
iSCAT	Interferometric scattering microscopy
NA	Numerical aperture
NTA	Nanoparticle tracking analysis
PAS	Propagation of angular spectrum
PEG	Polyethylene glycol
POPC	1-palmitoyl-2-oleoyl-sn-glycero-3-phosphocholine (lipid molecule)
PS	Polystyrene
PSF	Point spread function
RIU	Refractive index units
SLB	Supported lipid bilayer
STD	Standard deviation
TIRF	Total internal reflection fluorescence
WAC-NET	Weighted average convolutional neural network

Meaning of mathematical symbols

A,$\tilde{\lambda}$	Calibration parameters for two-dimensional flow nanometry
b	Slip length
D	Diffusion constant
D_∞	Diffusion constant in bulk (far away from any neighbouring surface)
δ	Characteristic decay length in TIRF
η	Viscosity
f	Optical form factor
$\boldsymbol{\mathcal{F}}$	Two-dimensional Fourier transform
h_0	Distance from the centre of a particle to a nearby surface
J_1	First order Bessel function
$\vec{k}$	Wave vector, $\left\vert\vec{k}\right\vert = \frac{2\pi}{\lambda}$
k_B	Boltzmann constant
K	Blur-factor describing the effect from particle motion during the exposure time
λ	Wavelength
m	Particle mass
μ	Mobility
n	Refractive index
N	Number of particle observations
σ^2	Contribution of localisation uncertainty to the mean squared displacement
$\Delta\Phi$	Optical phase-shift
R_h	Hydrodynamic radius
T	Temperature (in Kelvin)
v	Flow-induced velocity
γ	Friction coefficient
ξ	Stochastic force
ζ	Position uncertainty

1

Introduction

The inability to predict outliers implies the inability to predict the course of history.
– *Nassim Nicholas Taleb*

Life is a process outside thermal equilibrium where most of the underlying processes occur on nanometre to micrometre length scales (see Figure 1), and thus cannot be seen directly by the naked eye [1]. Nevertheless, visualisation is often key in order to understand complex systems, as best captured by the phrase *"seeing is believing"*. To overcome the limitations of the eye it is possible to use a microscope. Numerous microscopy techniques have for this reason been developed over the centuries, ranging from different optical methods to electron microscopy and atomic force microscopy [2–4]. Each development has increased the capability to investigate experimental systems, as recognized by more than five Nobel Prizes related to advances in the field.

Building on that tradition, the pursuit of ever better imaging tools continues to this day. However, just because it is possible to image a particular experimental system, interpreting the data correctly is far from a trivial task. An interpretation is always based on the current understanding of the world and the available tools to measure it. For example, in the beginning of the 19th century, Robert Brown and several other researchers observed that small particles, such as clay particles contained in the pollen of plants[*], display a stochastic motion[†] when dispersed in a fluid [5–7]. Numerous explanations for this phenomenon were initially hypothesised, and it was not until Albert Einstein's work about the subject it was settled that this motion originates from the existence of atoms and molecules [8]. Similar stories occur all the time, where new interpretations change the meaning of old data, illustrating the difficulty in decoding all the information which is present in a set of microscopy images of non-stationary particle systems.

The thesis you are currently reading has its core motivation in characterising the motion and optical signal of particles smaller than the wavelength of visible light, in particular

[*] Robert Brown wrote that he analysed particles or granules from grains of pollen [5].
[†] Commonly referred to as Brownian motion.

for non-idealised systems with confined diffusivity, non-trivial hydrodynamic boundary conditions and dynamically changing particle properties. Entities smaller than the wavelength of light are present in our everyday life. For example, as illustrated in Figure 1, single biomolecules typically are a few nanometres in size and the sizes of viruses and lipid vesicles span from a few tens of nanometres and upwards [1]. Moreover, dietary products often contain both emulsions and particles of nanoscopic and microscopic dimensions [9,10]. Such entities are often dynamically changing and are commonly located in complex and partially unknown environments, making quantitative characterisation of these entities a challenging task. As an example, the mobility of a particle depends not only on particle size, but also on its shape, the viscosity of the surrounding medium, proximity to neighbouring surfaces, hydrodynamical boundary conditions etc. [11–13]. Thus, if more than one of these experimental conditions are unknown or if any of them changes with time, accurate particle characterisation becomes a difficult task. One strategy to handle some of these challenges is to isolate the particles of interest in a known experimental environment. However, even if it would be possible to obtain the entities in a well-defined environment without affecting them during the process, which is not necessarily a simple task, the subsequent data analysis still requires several assumptions that often are challenging to evaluate due to lack of suitable experimental techniques. Thus, in a general sense, developing new means that increase our ability to investigate non-idealised systems bring forth the potential for unexpected discoveries across research fields, in addition to the particular information gathered about the investigated systems in question.

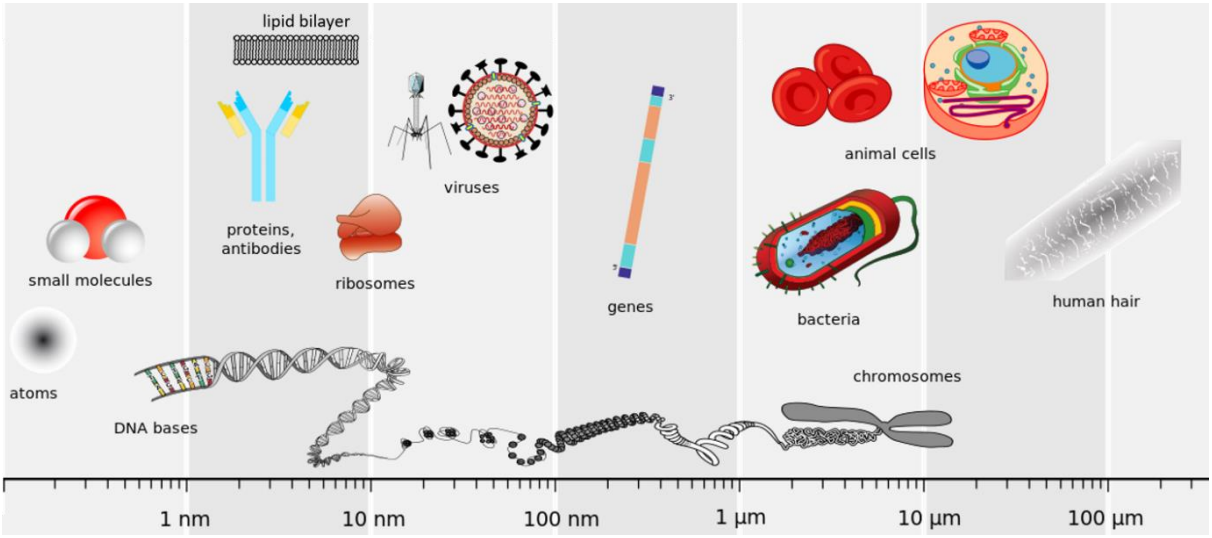

Figure 1: Schematic figure showing examples of important biological entities that occur on different length scales, ranging from sub-nanometre to hundreds of micrometres. The image is adapted from Wikimedia [14] under CC BY-SA 2.5 licence.

Although microscopy methods such as electron microscopy have a spatial resolution well beyond that of optical microscopy, the latter is still often preferred in the context of life sciences as it induces relatively little sample perturbations and enables imaging under physiological or near physiological conditions. In the specific case of characterising dielectric particles using optical microscopy, a possible analysis approach is to quantify radius and refractive index on the single particle level, as the combination of these properties relates to both particle size and mass [15–17]. Size and refractive index can be quantified by comparing the measured scattering pattern to theory describing the experimental system [18,19]. Despite its potential, the current implementations of this analysis approach are either limited to single observations [19], particles larger than the wavelength of light [20] or non-dynamic particle properties [17]. In several experimental systems, such as nanoparticle aggregation or particles inside living cells, it is of interest to follow the particle signal as it changes over time and over length scales ranging from single particles to larger aggregates. Some aspects of this challenge are handled in Paper I, where simultaneous characterisation of size and refractive index is extended to include subwavelength sized particles with a minimum size of $R = 150$ nm This was achieved by combining the recently developed off-axis holographic nanoparticle tracking (H-NTA) with deep-learning based Mie theory fitting [17,21]. In addition to accurately characterising multi-component particle samples without requiring information about the surrounding medium, the analysis approach enables changes in size and refractive index to be followed with a sub-second temporal resolution. The latter aspect of the method was used to show reversible signal changes for salt-induced clustering of polystyrene nanoparticles. These results illustrate the potential of using H-NTA to characterise dynamic particle systems that are challenging to analyse using alternative methods. Furthermore, preliminary data, presented in Sections 6.1-0, from our further developments of H-NTA show promising results regarding resolving dynamical signal changes for particles in complex backgrounds such as inside living cells, as well as decreasing the detection limit of optical holography by introducing off-axis twilight holography.

Even though it is possible to further decrease the particle size for which size and refractive index can be directly estimated from optical microscopy images, the limited spatial resolution of optical microscopy makes it a very challenging task [22]. However, if only size is of interest, it can be estimated by tracking the motion of particles in a fluid and relating the diffusion constant to size using the Stokes-Einstein relation [13].When relating diffusivity to particle size, several assumptions need to be made, one of which being directly connected to the particle's hydrodynamical boundary conditions. Typically, it is assumed that the fluid velocity parallel to the surface of the particle is zero at the particle-fluid interface, but this condition cannot be derived from first principles [12]. Since direct measurements of the boundary condition for nanoparticles are challenging using existing methods, the no-slip boundary condition is therefore commonly assumed without any evaluation of the validity of the assumption

for the particular system under investigation [12,23]. If no-slip is incorrectly assumed during diffusion-based sizing, the size becomes underestimated by up to approximately 30% [23]. Thus, there is a need for new experimental methods to evaluate the hydrodynamic boundary conditions for particles in general and for biological nanoparticles in particular, as the few existing methods either require significant buoyancy forces or that the particle size is significantly larger than the optical resolution limit [24–26]. To tackle this challenge, Paper II is focused on developing a method to quantify the boundary condition for biological nanoparticles. This was achieved by tethering biological nanoparticles to a mobile supported lipid bilayer (SLB, see Figure 1 for a schematic sketch) and quantifying the size-diffusion relation using the ratio between flow-induced velocity and diffusivity. By separating the respective friction contribution from the tethers and the particle, the size-diffusivity relation of the particle could be directly linked to the hydrodynamic boundary conditions. This technique was used to quantify partial-slip for different lipid vesicles, where the results indicate a difference in the size-diffusivity relation between synthetic lipid vesicles and cell-membrane derived vesicles. The latter difference is consistent with the expected influence of protruding membrane-bound molecules on cell-membrane derived vesicles [27]. The quantified size-diffusion relation also clarifies the mechanistic aspects concerning the mobility of membrane-attached nanoparticles, which is important both for the understanding of the initial lateral motion of viruses when attached to the cell surface as well as for the mobility quantification of membrane residing biomolecules when nanoparticles are used as tracing labels [28,29].

To provide the theoretical context of the work, this thesis begins with two chapters describing the theoretical background of the topics in this project. Thereafter a chapter covering the main experimental methods used in this work is presented, which is followed by a chapter summarising the two appended papers and a final chapter describing the future outlook of the project with references to additional experiments and ongoing method development.

2

Optical imaging theory

"The book is about how small particles absorb and scatter light."
"My goodness, who could possibly be interested in that?"[*] [30]

In both physics and science in general, theory and experiments are inescapably intertwined with each other. In essence, theory is used to predict and interpret experiments, while experiments that deviate from the current theoretical framework are used to guide future theoretical development. Since this thesis is based on analysing the motion and signal from subwavelength sized particles in optical microscopy images, the starting point in both cases is the analysis of a large set of images acquired through optical microscopy. Thus, in this chapter, the theoretical background for optical imaging is presented, with particular focus on the optical scattering from particles that are smaller than the wavelength of the incident light.

Theoretical discussions about optical measurement techniques tend to start with Maxwell's equations, which is a set of differential equations describing the spatiotemporal evolution of electromagnetic fields [31,32]. In principle, all classical properties of light can be derived from Maxwell's equations, although the solutions might be challenging to obtain. However, as microscopes were developed centuries before Maxwell's equations were first written down [33], there are several simplified models to explain the occurring physics [22,33]. The main benefits with the simplified explanations are that they aid in forming an intuition of the underlying physics and are often simpler to use than starting from Maxwell's equations, although the validity of the assumed approximations needs to be evaluated on a case-by-case basis. Thus, for a rigorous handling of Maxwell's equations, I refer to Jackson [31], Cheng [32] or any of the numerous books on the subject. Here, the theoretical discussion will instead be based around (i) the theory of optical wave propagation, which describes how light propagates from the sample to the measurement device [22], and (ii) the theory of optical scattering by small particles, which describes the signal originating from the sample [30].

[*] According to Google Scholar, by 2021-03-18 the book in question has been cited more than 29000 times.

However, before describing the theory of optical imaging, some fundamental properties of light need to be established. Although what our eyes and cameras typically register is the light intensity, which is proportional to the energy of the light source [32], it does not contain all the information needed to describe the propagation of light. Instead, the properties of light are described by its optical field, $\vec{E}(x, y, z)$, where the intensity is proportional to $\left|\vec{E}\right|^2$ [22]. In the context of optical imaging theory, the difference between the optical field and light intensity is that the optical field has a phase Φ and a polarisation.

Regarding the phase, as light propagates, the phase changes depending on the distance travelled, Δx, according to $\Delta\Phi \propto \Delta x/\lambda$, [22] where λ is the wavelength of light. Thus, for two optical fields which are coherent but that have travelled different distances before reaching the same spot, the corresponding phase difference will determine the resulting measured intensity (see Figure 3) [22,32]. This property of light is critical both for understanding the optical scattering signal from non-metallic particles (see Section 2.4) as well as for the working principle of off-axis holographic microscopy, which was the main experimental tool used in Paper I.

Regarding the polarisation, it describes the direction of the electric field as the electromagnetic wave propagates through space [22,32]. The direction of the polarisation is important both in the context of scattering from asymmetric particles as well as from the notion that optical fields with orthogonal polarisation will act as independent fields [22,30]. Thus, for spherical particles, the polarisation of the incoming light is of less importance than for asymmetric particle shapes as the scattering is independent of the particle orientation. Furthermore, the optical field has also a propagation direction, which in some instances is orthogonal to the direction of polarisation [31,32].

Taken together, when combining the properties of the optical field, we see that it has: an amplitude, phase, wavelength, polarisation, and a direction of propagation. These properties are all needed to fully describe the propagation of light, as will become apparent in the following sections. Also note that the classical description of light is here used, in which the properties of light are explained in the context of a continuous wave and not as a photon. Since an image typically involves measuring the contribution of numerous photons, the classical description of light describes the occurring physics well. Nevertheless, the discrete energy content from the photon is still needed to understand the process behind fluorescence. Thus, light will in the henceforth be described as electromagnetic waves with a discrete energy content.

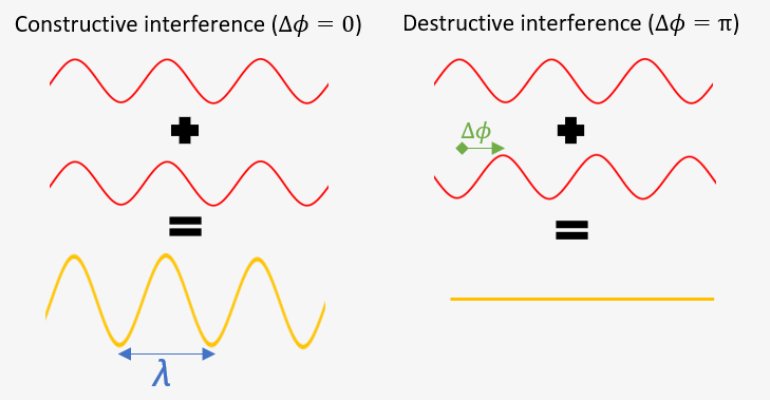

Figure 2: Schematic illustration of the interference properties of light waves. When two different light waves combine, depending on the phase difference $\Delta\Phi$ between the waves, the interference is either constructive or destructive. Note that the image shows the two extreme cases when $\Delta\Phi = N\pi$ and $\Delta\Phi = (2N-1)\pi$, where N is an integer. If $\Delta\Phi$ has any other value, the resulting interference will be in-between the two presented cases.

2.1 Huygens–Fresnel principle of wave propagation

The first well-established theory of optical wave propagation was derived by Huygens in the 17th century [33], which pre-dates Maxwell's equations with over a century [34]. The idea behind the Huygens–Fresnel principle of wave propagation is that the optical field can be deconstructed into wavelets* for which the equation for the optical propagation is known. If considering a wavelet at the starting position (x_0, y_0, z_0), then according to Huygens–Fresnel, the optical field at any other position is: [22]

$$E(x,y,z) \propto E_0(x_0,y_0,z_0)\frac{e^{-ikR}}{R}\left(1+\cos\left(\vec{R},\vec{k}_0\right)\right), \qquad 2.1$$

where $E_0(x_0,y_0,z_0)$ is the optical field at position (x_0,y_0,z_0), k is the wavenumber $(k = 2\pi/\lambda)$, $R = \sqrt{(x-x_0)^2+(y-y_0)^2+(z-z_0)^2}$, i is the complex unit and $\cos\left(\vec{R},\vec{k}_0\right)$ describes the angular amplitude profile between the direction of the incident wave and propagation direction. Note that polarisation of the field is dropped here as it does not influence the equations regarding propagation of light [22]. In essence, what Eq. 2.1 describes is a wavelet with a $\left[1+\cos\left(\vec{R},\vec{k}_0\right)\right]$ amplitude profile for which the phase scales linearly with the distance propagated and the field amplitude decreases as $1/R$, where the $1/R$ scaling comes from the fact that energy is conserved during propagation [32]. A visualisation of this propagation can be seen in Figure 3.

* A wavelet is a mathematical function used to deconstruct a given function or continuous signal into a superposition of functions with well-defined properties, a procedure that often is used in signal analysis.

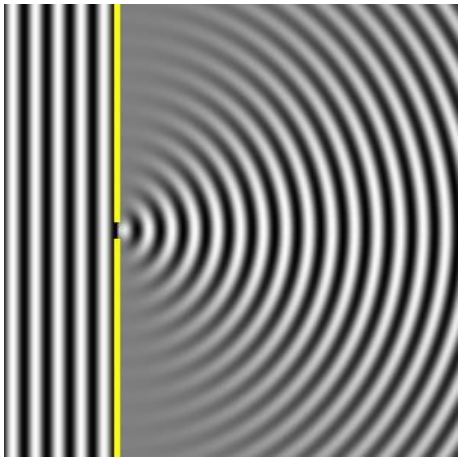

Figure 3: Illustration of the optical field from the wavelet used in the Huygens–Fresnel principle of propagation. The light comes from the left and impinges on an aperture (yellow line). The light which goes through the opening has the $\left[1+\cos\left(\vec{R},\vec{k}_0\right)\right]$ amplitude profile. The image is taken from Wikimedia [35] under CC BY-SA 3.0 licence.

Using Eq. 2.1 as a starting point, in the case of more than one wavelet, the resulting field is a sum of all the wavelets. This implies a linearity of the optical field, which is a central aspect both in Maxwell's equations and the Schrödinger equation [32,36]. Thus, the full optical field at an arbitrary imaging plane is mathematically expressed as:

$$E(x,y,z) = -\frac{i}{\lambda}\iint E(x',y',0)\frac{e^{-ikR}}{2R}\left(1+\cos\left(\vec{R},\vec{k}_0\right)\right)dx'dy', \qquad 2.2$$

where $R=\sqrt{(x-x')^2+(y-y')^2+(z-0)^2}$. Thus, it follows from Eq. 2.2 that if the optical field is known at any one plane, then the optical field at any other plane can be calculated. Note that the integral is evaluated for a 2D plane where the coordinate system is typically defined such that $z_0=0$, but any other choice of coordinate system is also valid.

However, Eq. 2.2 only describes the simplified situation of propagation in a constant environment. In most real-life situations, the imaging system contains several optical components such as lenses and apertures (see for example Figure 9 in Section 4.1.1). If an optical component is located along the path of the optical field, the subsequent propagation is affected. The mathematical procedure to handle this is to evaluate the optical field just before the component, calculate the change of the optical field induced by the component, and then initiate a new propagation after the component [22]. Thus, performing all the mathematical operations becomes challenging to perform analytically for optical systems with more than just a few components.

Although Eq. 2.2 can be used to describe the optical propagation in several important special instances, Eq. 2.2 is based on approximations which limits its applicability. First, Eq. 2.1 diverges as $R\to 0$. Thus, it primarily describes the propagation over distances much longer than the wavelength of light [15,22]. Second, to solve Eq. 2.2 analytically it is often combined with the paraxial approximation; in which only small angles in relation to the direction of the incoming field are considered [15,22]. For these

reasons, other approaches have been developed which do not contain these approximations, particularly when solving the equations numerically using a computer. Nevertheless, the Huygens–Fresnel principle is still useful for calculations of the optical field over long distances and to understand the mathematical structure of other calculation strategies [15,22].

2.2 Propagation of angular spectrum

An alternative starting point to the wavelet used in the Huygens–Fresnel principle is the plane wave solution to Maxwell's equations. In free space, Maxwell's equations become the Helmholtz equation: [32]

$$\nabla^2\vec{E}(x,y,z) + k^2\vec{E}(x,y,z) = \vec{0}, \qquad 2.3$$

which has the solution $\vec{E}(x,y,z) = \vec{E}_0 e^{-i(\vec{k}\cdot\vec{r})}$, where $\vec{k}$ is the wave vector that defines the direction of propagation and $|\vec{k}| = k = 2\pi/\lambda$. This solution is often referred to as the plane wave solution, as the optical field is constant over a plane orthogonal to the wave vector. Using the plane wave solution as a basis, any optical field in free space can be written as sum of plane waves as: [15]

$$\vec{E}(x,y,z) = \iint_{k_x^2+k_y^2\leq k^2} \vec{A}(k_x,k_y) e^{-i\left(k_\mathrm{x}\cdot x + k_\mathrm{y}\cdot y + \sqrt{k^2-k_\mathrm{x}^2-k_\mathrm{y}^2}\cdot z\right)}\,\mathrm{d}k_\mathrm{x}\mathrm{d}k_\mathrm{y}, \qquad 2.4$$

where $\vec{A}(k_\mathrm{x},k_\mathrm{y})$ is the amplitude of the plane wave corresponding to the value of k_x and k_y. Note that since $|\vec{k}|^2 = k_x^2 + k_y^2 + k_z^2 = (2\pi/\lambda)^2$, for each choice of k_x and k_y the magnitude of k_z is also determined. Thus, the integral is only evaluated over k_x and k_y, where the range of allowed values are limited by the criterion $|\vec{k}|^2 = (2\pi/\lambda)^2$.

When inspecting Eq. 2.4, its structure is similar to that of the two-dimensional Fourier transform [37]. Thus, Eq. 2.4 can be written as:

$$\vec{E}(x,y,z) = \boldsymbol{\mathcal{F}}\left(\vec{A}(\vec{k}) e^{-i\sqrt{k^2-k_\mathrm{x}^2-k_\mathrm{y}^2}\cdot z}\right), \qquad 2.5$$

where $\boldsymbol{\mathcal{F}}$ is here used to describe the two-dimensional Fourier transform operator for the function inside the parenthesis. By applying the inverse Fourier transform to Eq. 2.5:

$$\vec{A}(\vec{k}) e^{-i\sqrt{k^2-k_\mathrm{x}^2-k_\mathrm{y}^2}\cdot z} = \boldsymbol{\mathcal{F}^{-1}}\left(\vec{E}(x,y,z)\right). \qquad 2.6$$

Thus, in a similar way to the Huygens–Fresnel principle, if the optical field is known at any one plane, $\vec{A}(\vec{k})$ can be obtained using Eq. 2.6. Once $\vec{A}(\vec{k})$ is known, the optical field for any other plane is also known by the use Eq. 2.5. This way of numerically

propagating the optical field is called propagation of angular spectrum (PAS) [15]. The benefits of PAS compared to Huygens–Fresnel are that (i) it is possible to propagate the field over short distances, (ii) it is a more general formalism of the optical field, and (iii) the propagation can be calculated using Fourier transforms, which are fast operations on modern computers. For this reason, PAS is the method used to numerically propagate the optical fields in the off-axis holography work related to this thesis.

2.3 Optical resolution limit

When inspecting Eq. 2.4, the integral is carried out over a finite set of k_x and k_y values, where the largest k value is set by the wavelength. Since the k value is related to the resolution, with larger k values leading to reduced widths of the signal distribution [37], the wavelength determines the optical resolution in case of ideal imaging. Thus, an optical microscope acts as a low-pass spatial frequency filter.

To exemplify this, the Fourier transform of an idealised point source is constant over all frequencies. The inverse transform using the optically available spatial frequencies, $k_{\mathrm{x}}^2 + k_{\mathrm{y}}^2 \leq k^2$, results in the optical field $\vec{E}(\rho) \propto \frac{J_1(\rho k)}{\rho k}$, where $\rho^2 = x^2 + y^2$ and J_1 is the first order Bessel function [22,37]. Thus, although the object itself is an idealised point source, an image of the object will have a finite width set by the highest spatial frequencies that the microscope can capture. This is further exemplified in Figure 4, where the effect on a subwavelength-sized sphere is shown.

At this point it is important to distinguish between detecting a particle and resolving a particle. As long as the optical signal is sufficiently large, a particle is detectable in a microscope no matter its geometrical size. However, to resolve a particle it needs to be distinguished from potential neighbouring particles. If two objects are close enough such that their optical signals spatially overlap, then at a certain distance they will no longer be distinguishable [22]. The shortest distance for which the individual particles are distinguishable is referred to as the resolution limit. The commonly used expression for the resolution limit is $\frac{0.61\lambda}{NA}$ [22], where NA is the numerical aperture and is related to the highest spatial frequency a microscope can capture for a certain wavelength. The definition of the resolution limit may vary between different optical techniques as it depends on the details of the recorded signal [38], but as a rule of thumb the limit is on the order of $\frac{\lambda}{NA}$.

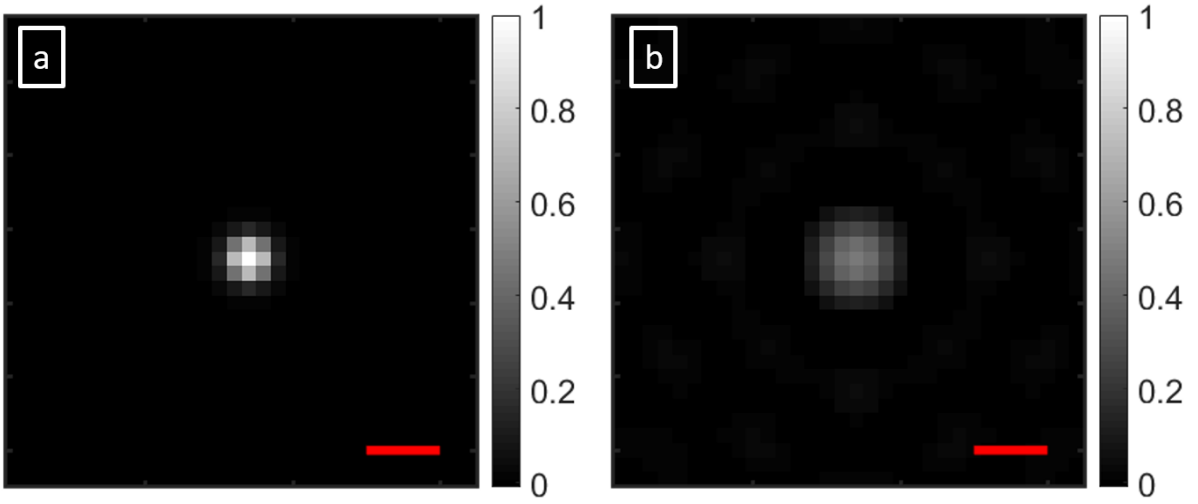

Figure 4: Example of the low-pass filter effect from optical microscopy using numerical calculation of a 100 nm diameter spherical particle and a wavelength of 635 nm. (a) is the initial particle signal and (b) is the particle signal when only spatial frequencies fulfilling $k_x^2 + k_y^2 \leq \left(\frac{2\pi}{\lambda}\right)^2$ are included. The colorbars represent the amplitude of the optical field from the particle, normalised such that the maximum value before the filtering is equal to 1. The scalebars correspond to 500 nm.

2.4 Optical signal from small particles

In a homogenous environment, light propagates as described in Section 2.2, where the only distance dependent factor is $e^{-i\sqrt{k^2-k_x^2-k_y^2}\cdot z}$ (see Eq. 2.4). For Eq. 2.4 to be valid, the refractive index needs to be the same across the region where the optical field is located. Following this reasoning, for deviations from ordinary optical propagation to occur, as for example optical scattering, there needs to be spatial variations for the refractive index [30].

The underlying physical principle behind optical scattering is that matter is composed of electrical charges, and that an incident electromagnetic field induces an oscillatory motion of these charges [32]. These oscillatory motions in turn act as antennas which take energy from the incident field and redirect it, causing scattering of light [32]. In a homogenous environment, the backward and forward scattering from different regions balance each other. However, when light transitions between materials with different abilities to generate these field-induced dipoles, i.e. materials with different refractive index, the scattering from different regions will no longer cancel each other out [32].

In a similar way to the propagation of light, where the optical field is described by a superposition of wavelets, the scattering from a small* weakly optically interacting† particle can be described by subdividing it into smaller regions where the scattering

* Small here refers to a comparison with the wavelength of the incident light.
† Weakly optical interacting particle here means that the absolute difference in refractive index between the particle and the surrounding medium is much smaller than one.

from each subregion acts as a wavelet [30]. Scattering from a particle in the point-like limit is: [30]

$$\vec{E}_{\mathrm{s}} = \frac{e^{-\mathrm{i}\vec{k}\cdot\vec{R}}}{-ikR} S \begin{pmatrix} \cos(\theta) & 0 \\ 0 & 1 \end{pmatrix} \vec{E}_{\mathrm{in}}, \qquad 2.7$$

where $\vec{E}_{\mathrm{in}}$ is the incident optical field and θ is the angle between the directions of the incident and scattered optical field (see Section 2.1), while

$$S = -v \frac{3ik^3}{4\pi} \frac{n_{\mathrm{p}}^2 - n_{\mathrm{m}}^2}{n_{\mathrm{p}}^2 + 2n_{\mathrm{m}}^2}, \qquad 2.8$$

where n_{p} is the refractive index of the particle, n_{m} is the refractive index of the surrounding medium and v is the volume of the point-like particle element. The scattering from the full particle is the sum of the field contributions originating from all subdivided regions. In the case of a small weakly optically interacting particle, it is typically assumed that the excitation for each subdivided region is caused only by the incident optical field, thus neglecting influence from neighbouring subdivided regions [30]. With this assumption, the particle scattering is the same as Eq. 2.7 except for a correction factor f, typically referred to as the form factor, which describes the interference in the far-field from the different subdivided regions of the particle [30]. Mathematically, f is expressed as:

$$f(\theta, \Phi) = \frac{1}{V} \int_V e^{-i\Delta\phi} \, \mathrm{d}v, \qquad 2.9$$

where V is the full particle volume and $\Delta\phi$ is the phase difference of the light contributions originating from the subregion $\mathrm{d}v$ to the observation direction, where the angles θ and Φ indicate that f depends on both the direction of the incident light and the direction of the scattered light. This approximation of optical scattering from small particles is often referred to as Rayleigh-Gans theory. From this expression, the contribution from various particle shapes can be readily estimated as long as the assumption of small weakly optically interacting particles is valid [30]. For example, from these equations the change in optical scattering signal from deformation of lipid vesicles can be estimated and compared with the change in fluorescence signal [39].

In the case of spherical particles, there exists a complete solution without the assumption of small weakly optically interacting particles. This solution was first derived by Gustav Mie and is commonly referred to as Mie theory [40], and is applicable for both dielectric particles and metallic nanoparticles [18,40]. Mie theory solves the optical scattering as an infinite sum of spherical polynomials [40], and is thus primarily used for numerical calculations whereas Rayleigh-Gans theory is easier to use when deriving analytical expressions.

Although Eqs. 2.7-2.9 at first glance present themselves as mathematically cumbersome, there are some rules of thumb that can be used to interpret the magnitude of the optical signal in some important special cases. First, if the particle is small enough

such that the shape factor can be approximated as 1, then the optical field scales with particle volume. This scaling is important both in the context of understanding the limit of detection for different microscopy techniques and in relating the signal amplitude to particle properties. For example, this approximation is used to optically quantify the mass of single biomolecules using a microscopy method called interferometric scattering microscopy (iSCAT) [41,42]. Second, if the particles are large enough to be described by geometrical optics, the integrated phase shift induced by a particle is proportional to $V\Delta n$ [17,43]. This property enables optical measurements of the dry mass of cells as well as analysis of sub-micron gas bubbles in water [17,43]. Thus, both in the limit of very small and large particles, experimentally accessible properties of the optical field scale with particle volume and the refractive index.

2.5 Fluorescence

In scattering-based optical microscopy, as detailed in Section 2.4, all heterogeneity in the spatial distribution of the refractive index will contribute to the optical signal. Thus, label-free scattering-based microscopy naturally lacks specificity, which in some cases is disadvantageous.

To obtain a specific optical signal with high spatial resolution, the most common technique is fluorescence. Fluorescence is a subclass of luminescence, which is the process where light is emitted from electronically excited states [44]. In fluorescence, the initial excitation originates from absorption of a photon at a particular wavelength and the subsequently emitted photon typically has a lower energy than the incident photon [44]. This shift in energy originates from that the excitations are linked to a vibronic transition, in which the molecule changes both its electronic and vibrational state, a process this is often visualised using a Jablonski diagram (see Figure 5) [44,45]. Since vibrational relaxations occur on a faster time scale than the electron relaxation, the vibrational relaxations will cause the emitted photon to have lower energy than the initially absorbed photon [44,45].

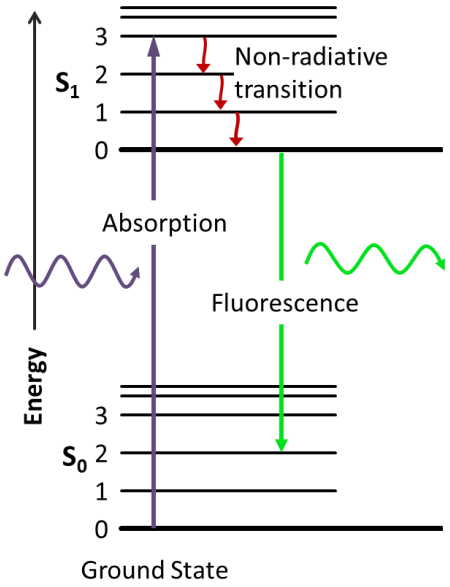

Figure 5: Jablonski diagram. An incoming photon at a particular wavelength is absorbed, which changes both the electronic and vibrational state of the molecule. The electronic state is indicated by S_i and the vibrational state is the number next to each plateau. Since the vibrational relaxations occur on a faster time scale than the electron relaxation, the system will relax to the lowest vibrational state before emission of a photon at a lower wavelength than the initial excitation. The image is adapted from Wikimedia [46] under CC0 1.0 licence.

3

Brownian motion

The story of Brownian motion is one of confused experiment, heated philosophy, belated theory, and, finally, precise and decisive measurement
- *M D Haw, 2002* [6]

One of the most prominent examples of the intertwined relationship between experiment and theory is Brownian motion, where over a century of research is captured by the quote in the beginning of this chapter. When following the motion of particles that are free to move around in a viscous fluid, one part is deterministic, and another will appear to be stochastic. The stochastic part of the motion is commonly referred to as Brownian motion. This phenomenon was observed by several researchers during the 19th century [6], but the name of Robert Brown has become synonymous with the process [5]. For a long time the origin of this phenomenon was unknown, but during the 20th century it was settled that Brownian motion is due to random collisions between the particle and molecules in the surrounding fluid [8]. Nevertheless, relating Brownian motion to particle properties is generally not a simple task since several assumptions need to be made, where some of the assumptions are difficult to evaluate experimentally. For a general treatment of the hydrodynamics of particles in a fluid I refer to Happel and Brenner [47]. In this chapter, the theoretical discussion will focus on Brownian motion and its dependence on hydrodynamic boundary conditions, confinement and tethering to a fluid surface.

After Einstein's initial derivation, several equations describing Brownian motion have been developed, for example the Langevin equation and the Fokker-Planck equation [48]. Starting from Newton's equation of motion, the motion of a particle with a low Reynolds number* is given by the equation: [47]

$$m\frac{dv(t)}{dt} = -\gamma(v(t) - v_{\text{fluid}}), \qquad 3.1$$

* Solutions to the Navier-Stokes equation exist only in a few special cases. One common approximation is assuming slow viscous flow, in which viscous forces dominate over inertial forces. This approximation is valid for particles dispersed in a fluid when the Reynolds number, (fluid density)×(velocity)×(size)/(viscosity), is smaller than 0.05 [47].

where γ is the friction coefficient from the fluid acting on the particle, m is particle mass and v_{fluid} is the bulk velocity of the fluid. From Eq. 3.1, it follows that $v(t) \rightarrow v_{\text{fluid}}$ as $t \rightarrow \infty$. However, one central concept in statistical physics is thermal fluctuations. In particular, the equipartition theorem states that if a system is in thermal equilibrium, every independent energy term has a mean value equal to $\frac{1}{2}k_{\text{B}}T$, where k_{B} is Boltzmann's constant and T is the temperature in Kelvin [48]. Translated to the case of Eq. 3.1, the equipartition theorem states that $< v^2 >$ * should be different from zero as $t \rightarrow \infty$, which clearly is not the case if $v_{\text{fluid}} = 0$. Since the motion of the particle should be consistent with the equipartition theorem, Eq. 3.1 does not correctly describe the full motion of a particle immersed in a fluid.

The overlooked contribution to the particle motion in Eq. 3.1 is that molecules in the fluid may bump into the particle such that it gains velocity, an effect that is typically described as a stochastic force. As a general phenomenon in physics, whenever there is a dissipative force, such as friction between a particle and the surrounding fluid, there is also a stochastic force, a relation known as the fluctuation-dissipation theorem [48,49]. When adding a stochastic force to Eq. 3.1, which changes Newtons equation to the Langevin equation, the equation of motion becomes:

$$m\frac{dv(t)}{dt} = -\gamma(v(t) - v_{\text{fluid}}) + \xi(t), \qquad 3.2$$

where $\xi(t)$ describes the stochastic force. In the case of experimental measurements of Brownian motion, the time in-between position measurements is typically much longer than the time in-between collisions of the particle with the molecules in the fluid [48]. This observation implies that $\xi(t)$ can be approximated as:

$$< \xi(t) >= 0 \text{ and } < \xi(t_1)\xi(t_2) >= 2B\delta(t_1 - t_2), \qquad 3.3$$

where $\delta(t)$ is the delta function, which is zero for all t except for t close to zero. In other words, Eq. 3.3 implies that the stochastic force has a mean value equal to zero and no time correlation. Interestingly, to make Eq. 3.2 consistent with the equipartition theorem, $B = \gamma k_{\text{B}}T$ [48]. This relation between γ and B exemplifies the relation between the dissipation and stochastic aspects of the system, showing that the two are intrinsically interlinked with each other.

* Angle brackets here stands for the time average of what inside the brackets.

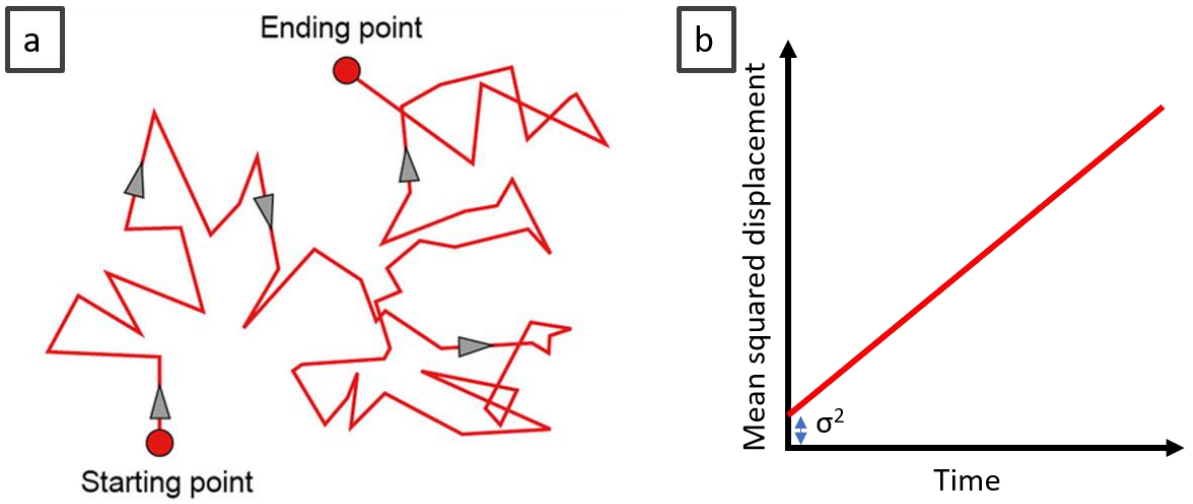

Figure 6: Schematic images describing Brownian motion. (a) Plot of the particle postion at discrete time steps. (b) The mean squared displacement ($< (x(t) - x_0)^2 >_T$) over time, which is linear for ordinary Brownian motion (see Eq. 3.5). The slope relates to the diffusion constant of the particle and the offset σ^2 from origin relates to position uncertainty (see Section 3.4). (a) is taken from Wikimedia [50] under CC BY-SA 4.0 licence.

Brownian motion is most often quantified using mean squared displacement, $< (x(t) - x_0)^2 >$. The derivation of the expression for the mean squared displacement starting from Eqs. 3.2-3.3 is outlined in several books about the subject [48], and will not be reproduced here. Using the end-result of such derivations, the mean squared displacement when the particle is in equilibrium with the fluid is: [48]

$$< (x(t) - x_0)^2 >_T = \frac{2k_B T}{\gamma}\left[t - \frac{m}{\gamma}\left(1 - e^{-(\gamma/m)t}\right)\right]. \qquad 3.4$$

If the inertia of the particle is neglected, the mass-dependent terms in Eq. 3.4 can be dropped, which simplifies Eq. 3.4 to

$$< (x(t) - x_0)^2 >_T = \frac{2k_B T}{\gamma} t = 2Dt, \qquad 3.5$$

where $D = \frac{k_B T}{\gamma}$ is the diffusion constant. From Eq. 3.5 it follows that the mean squared displacement scales linearly with time, allowing the diffusion constant to be quantified from a linear fit [13,51].

In the case of a freely diffusing spherical particle, the diffusion constant is in turn related to its hydrodynamic radius R_h via the Stokes-Einstein equation,

$$D = \frac{k_B T}{6\pi R_h \eta}, \qquad 3.6$$

where η is the viscosity of the fluid [47]. Note the inverse relation between the diffusion constant and viscosity, which further exemplifies the relation between fluctuation and dissipation. Thus, by estimating the mean squared displacement it is possible to quantify its hydrodynamic radius, even when the size of the particle is well below the resolution

limit (see Section 2.3). However, the hydrodynamic radius is not necessarily the same as the geometrical radius R. This difference is further discussed in Section 3.1.

3.1 Hydrodynamic boundary conditions

Hydrodynamics follows the Navier-Stokes equations, which are a set of partial differential equations describing the motion of viscous fluids [47]. However, the hydrodynamic boundary conditions cannot be derived from first principles [12]. Instead, the boundary conditions need to be assumed or based on measurements. For macroscopic systems, the exact boundary conditions have only very minor influence on the overall system. But as the dimensions of the system become smaller, as is the case for diffusing nanoparticles, the boundary conditions may significantly affect the relation between the size and diffusion constant [23]. In addition to slip, in the case of charged particles in a ionic solution, some of the ions may follow the motion of the particle, which further affects the diffusion-size relation [52,53]. Thus, relating the diffusion constant to the geometrical size is, in general, a far from trivial task.

The boundary condition is typically divided into three cases: no slip, partial slip and perfect slip, as schematically exemplified in Figure 7. The most commonly used is the no slip boundary condition, in which case the velocity of the fluid parallel to the surface is zero at the transition between the fluid and the solid interface [12]. No slip is frequently observed for hydrophilic surfaces [54]. Since nanoparticles require hydrophilicity for a good dispersion in water or serum in order to prevent aggregation, no slip is therefore commonly assumed unless the surface has been modified to make it hydrophobic [55].

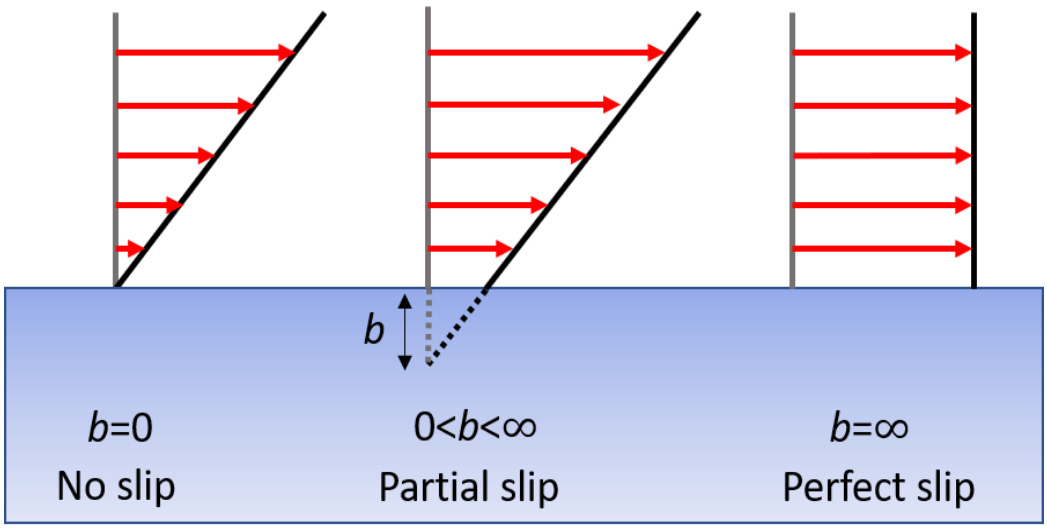

Figure 7: Schematic illustration of three common hydrodynamic boundary conditions. No slip: the velocity of the fluid parallel to the surface is zero at the transition between the fluid and the solid interface. Partial slip: the friction at the fluid-solid boundary is finite, causing the velocity of the fluid to behave as if the no slip boundary condition still occurs but for an effective surface which is inside the solid material, where the distance to effective surface is referred to as the slip length b. Perfect slip: the special case when the slip length is infinite.

A larger of class of hydrodynamic boundary conditions, in which no slip is just a special case, is partial slip, where the friction at the fluid-solid boundary is finite [12]. During partial slip, the velocity of the fluid behaves as if the no-slip boundary condition still occurs but for an effective surface inside the solid material. The distance between the true and the virtual interface is referred to as the slip length b, as illustrated in Figure 7. Experimental measurements of the slip length, using for example a surface force apparatus, range from nanometres to a few micrometres, where the general trend is that the slip length increases with increasing hydrophobicity and surface roughness [54]. Perfect slip, in contrast, is a special case of partial slip that is characterised by a slip length that approaches infinity, which is a useful approximation when the slip length is much longer that the length scale of the system [56].

The existence of non-zero slip is not only of theoretical importance; it also affects the relation between experimental results and physical properties of the system. For example, in the case of diffusing spherical particles, a non-zero slip changes the standard Stokes-Einstein equation to: [23,56]

$$D_{\mathrm{b}} = \frac{R+3b}{R+2b}\frac{k_{\mathrm{B}}T}{6\pi\eta R}, \qquad 3.7$$

where R is the geometrical size of the particle. Thus, the relation between the diffusion constant and particle size can change up to a factor of 3/2 depending on the relative length of the slip and the size of the particles.

3.2 Confined particle diffusion

The ordinary expression for Brownian motion assumes that the particle is far away from any neighbouring surface. If that is not the case, for example when a particle approaches a surface, its diffusion changes and becomes dependent on whether the motion is parallel or perpendicular to the surface [13,56]. This dependence comes from that when a particle moves it needs to displace the surrounding fluid. Consequently, confinement decreases the available pathways for the displaced fluid. The equation describing the change in diffusion constant parallel to the surface, when the particle is far away[*] from a planar surface under no-slip boundary conditions, was first derived by Hiding Faxén in the beginning of 20$^{\mathrm{th}}$ century [57]. Faxén's derivation is based on the method of reflections and is only an approximate solution, where different publications often include a different number of correction terms [13,47]. Using the 5$^{\mathrm{th}}$ order correction, the particle diffusion parallel to the surface is: [47,57,58]

$$D_{\mathrm{NP,int}} \approx D_{\infty}\left[1 - \frac{9}{16}\left(\frac{R_{\mathrm{h}}}{h_0}\right) + \frac{1}{8}\left(\frac{R_{\mathrm{h}}}{h_0}\right)^3 - \frac{45}{256}\left(\frac{R_{\mathrm{h}}}{h_0}\right)^4 - \frac{1}{16}\left(\frac{R_{\mathrm{h}}}{h_0}\right)^5\right], \qquad 3.8$$

where D_{∞} is the diffusion coefficient for the particle in bulk and h_0 the distance from the centre of the particle to the surface. This equation predicts that the closer the particle

[*] Far away here means that the distance to the surface is much longer than the size of the particle.

is to the surface, the slower the diffusion becomes. However, since Eq. 3.8 is derived for the case when $R_h/h_0 \ll 1$, its predictions becomes unreliable when $R_h/h_0 \to 1$. In this limit, the particle motion is better described by the equations derived for the lubrication regime [59]. To interpolate between the regimes, Brenner derived an equation that is commonly referred to as the Brenner formula [13,60], in which the particle diffusion parallel to the surface is:

$$D_B \approx D_\infty \left[1 - \frac{8}{15}\ln\left(1 - \frac{R_h}{h_0}\right) + 0.029\frac{R_h}{h_0} + 0.04973\left(\frac{R_h}{h_0}\right)^2 - 0.1249\left(\frac{R_h}{h_0}\right)^3\right]^{-1}. \quad 3.9$$

Although Eq. 3.8 and Eq. 3.9 are significantly different from each other, their predictions are similar as long as $R_h/h < 0.8$, which can be observed when visually comparing the relations, as shown in Figure 8 [59].

Confined diffusion is here treated under the assumption that the no slip condition applies. However, partial slip might occur at both the particle and the nearby surface, as reported for lipid bilayers using a surface force apparatus [61]. The resulting particle diffusion in the case when slip occur at both interfaces is not well established, especially when the distance from the particle to surface is comparable to the slip length [56]. In the limit where $h_0 \gg b$, the effect from the slip can be included in Eq. 3.8 by simply replacing h_0 with an effective distance $h_{ef} \equiv h_0 + b$. Thus, when the slip lengths are short, the hydrodynamics can be approximated by shifting the no-slip boundary below the interfaces, which was the approximation used in Paper II.

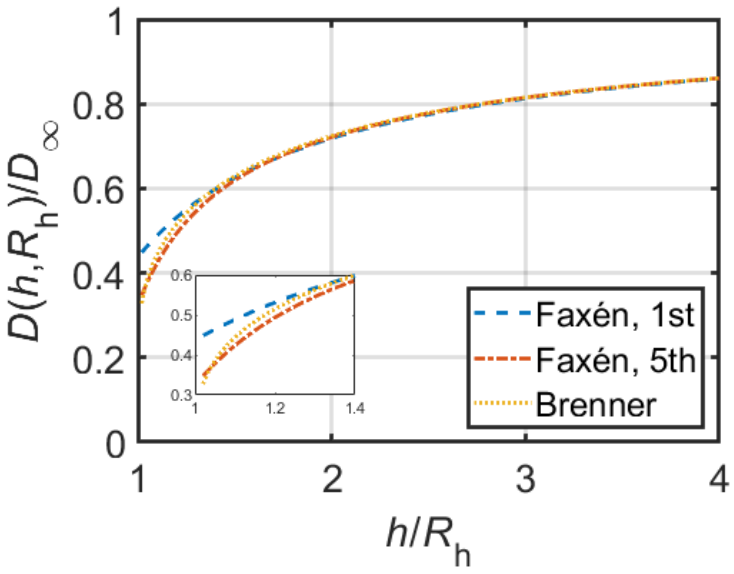

Figure 8: Plot of how the particle diffusivity parallel to a planar surface when assuming no slip decreases as a function of distance to the surface. The inset shows the difference between the three expressions, which primarily occur while $h/R_h < 1.3$.

3.3 Brownian motion of nanoparticles tethered to a lipid bilayer

When a particle binds to a receptor in a fluid-phase lipid bilayer, its subsequent diffusion depends not only on the confined particle diffusion but also on the mobility of the receptor. For nanoparticles, which in bulk have a much higher diffusion constant than molecules in the lipid bilayer [62], it is typically assumed that the diffusion constant of the tether-nanoparticle complex is set by the tethers in the lipid bilayer [63,64]. However, as demonstrated by Liao et. al. [65], particles with diameters as small as 15-20 nm significantly reduce the overall diffusion of the tether-nanoparticle complex if the number of tethers are few. Thus, the validity of the commonly used approximation that the nanoparticle contribution to the diffusivity is neglectable can be questioned.

In general, the diffusion of the combined nanoparticle-tether complex depends on both the nanoparticle mobility μ_{NP} and the mobility of the tethers μ_{T}, where the mobility is related to the diffusion constant as $\mu = Dk_{\mathrm{B}}T$. In the case of nanoparticles tethered to a lipid bilayer, μ_{NP} and μ_{T} are determined by two approximately independent frictions: between the surrounding fluid and the nanoparticle, and between the tethers and the lipids. Given that the frictions are inversely proportional to mobilities, the combined nanoparticle-tether mobility is:

$$\mu^{-1}(R_{\mathrm{h}}) = \mu_{\mathrm{NP}}^{-1}(R_{\mathrm{h}}) + \mu_{\mathrm{T}}^{-1}. \qquad 3.10$$

From Eq. 3.10 the diffusion constant is partly set by the nanoparticle itself and partly set by the tethers. Furthermore, under the assumption of independent forces, only one of the two terms in Eq. 3.10 is dependent on particle size. This observation is one of the underlying principles behind Paper II, as it allows for a strategy to separate the two terms in Eq. 3.10. In particular, since the number of tethers can only obtain discreate values, it is possible to distinguish between particles linked with one, two or more tethers. Combined with simultaneous size and diffusion constant measurement, achieved using two-dimensional flow nanometry (2DFN, see Section 4.2), the different terms in Eq. 3.10 could be compared to theoretical expressions using the slip length as a fit parameter.

3.4 Estimation of diffusion constant from particle tracking

As explained in Section 3, the diffusion constant of a particle is related to its size, where the exact size-diffusivity relation depends on several factors such as confinement and hydrodynamic boundary conditions. Nevertheless, no matter the correction factor, the first step is to quantify the diffusion constant using a set of estimated particle positions.

In the case of single-particle tracking combined with optical microscopy, the diffusion constant is most often estimated using the mean squared displacement [13]. The estimated particle position, $\hat{x}_{\mathrm{est}}(t)$, is a combination of the true particle position, $x_{\mathrm{true}}(t)$, and the experimental/analytical position uncertainty $\zeta(t)$, and is expressed as:

$$\hat{x}_{\mathrm{est}}(t) = x_{\mathrm{true}}(t) + \zeta(t). \quad 3.11$$

The position uncertainty depends on two different contributions: (i) how well the used position estimation algorithm can identify the centre of the particle, which varies depending on particle size and signal-to-noise ratio [66], and (ii) how much the particle moves during the exposure time. These two contributions affect the mean squared displacement differently, which according to Ref [51]* can be defined as:

$$< (\hat{x}_{n+1} - \hat{x}_n)^2 > = 2D\Delta t + 2(\sigma^2 - 2DK\Delta t), \quad 3.12$$

$$< (\hat{x}_{n+2} - \hat{x}_{n+1})(\hat{x}_{n+1} - \hat{x}_n) > = -(\sigma^2 - 2DK\Delta t), \quad 3.13$$

$$< (\hat{x}_{n+1} - \hat{x}_n)(\hat{x}_{m+1} - \hat{x}_m) > = 0 \text{ for } |m - n| > 1, \quad 3.14$$

where σ is the localization uncertainty, the subscripts correspond to independent particle observations, Δt is the time between the observations and K is the blur-factor describing the effect from particle motion during the exposure time. If the exposure time for the camera is the same as the time between frames, then $K = 1/6$ [67]. Thus, although σ^2 can be minimized using accurate localisation algorithms, the mean squared displacement will still deviate significantly from the diffusion constant if the exposure time is similar to the time between frames.

From Eqs. 3.12-3.13 it follows that it is possible to correct for the bias terms on the single particle level. However, the estimate is uncertain as the variance depends on the track length as: [51]

$$\mathrm{var}(\Delta x_n \Delta x_m) = \frac{\alpha + 4\alpha\beta + 6\beta^2}{N - |n-m|} - \frac{2\beta^2}{(N - |n-m|)^2}, \quad 3.15$$

where $\alpha = 2D\Delta t$, $\beta = \sigma^2 - 2DK\Delta t$ and $(N + 1)$ is the number of position observations of the same particle. If $\alpha \gg \beta$, for large N it follows from Eq. 3.15 that (standard deviation)/mean $\propto 1/\sqrt{N}$, which is the rule of thumb when it comes to diffusion estimation from particle traces. For this reason, it is beneficial to have long track lengths as well as performing the estimate of $(\sigma^2 - 2DK\Delta t)$ on the ensemble level. In Paper II, the correction was performed on the ensemble level using a linear fit between $< (\Delta x_n)^2 >$ and $< \Delta x_n \Delta x_{n+1} >$. This strategy was used since the particles all had a similar optical signal, making σ^2 approximately the same for the analysed particles. Thus, the main difference between the particles was their motion during the exposure time. In Paper I, since the size estimate was performed directly using the optical scattering signal, such corrections were not needed, which shows one of the benefits of not relying on estimates of the diffusion constant when quantifying particle properties such as size.

* In Ref [51], R is used instead of K, where K is here used to avoid confusion with the particle radius.

4

Experimental methods

If it disagrees with experiment it is wrong.
In that simple statement is the key to science.
– Richard Feynman

When measuring properties of macroscopic objects, such as the size of a football, it is typically assumed that the considered property can be measured without any restrictions from the tool itself. However, this reality changes when the size of the object becomes comparable to the resolution and/or the sensitivity of the measurement method. To tackle this problem, one approach is to work with method development, and another is to use complimentary measurement techniques. This thesis is founded in the former of the two. In this chapter, the details of the used experimental techniques are presented together with the complimentary techniques also used to evaluate their performance.

4.1 Quantitative phase microscopy

The information in an ordinary image recorded by a camera is related to the amplitude of the incoming light. However, as described in Section 2, the optical field has both an amplitude and a phase. The first microscopy technique measuring the phase signal was developed in the middle of the 20th century by Frits Zernike, in which a phase-delay ring was used to increase the contrast of weakly optically interacting samples [68,69]. Due to the information content in the phase signal, a vast number of phase microscopy methods have since been developed, all sharing some central features about how the phase information is obtained from images, which themselves only contain amplitude information.

The central idea to recover phase information is to relate the amplitude modulation of interfering optical fields to the phase content. If two or more optical fields are present at a camera, the recorded light intensity is:

$$I_{\text{cam}} \propto \left|\sum_n \vec{E}_n\right|^2 = \sum_n |\vec{E}_n|^2 + \sum_{n,m,n\neq m} \vec{E}_n \cdot \vec{E}_m^*, \qquad 4.1$$

where $\vec{E}_m^*$ is the complex conjugate of the optical field [22,32]. In the special case of two coherent optical fields* where one of the fields is a plane wave, $\vec{E}_0 e^{-i(\vec{k}\cdot\vec{r})}$ (see Section 2.2), then Eq. 4.1 can be expressed as:

$$I_{\text{cam}} \propto \left|\vec{E}_0 e^{-i(\vec{k}\cdot\vec{r})} + \vec{E}_n(\vec{r})\right|^2 = \left|\vec{E}_0\right|^2 + \left|\vec{E}_n(\vec{r})\right|^2 + \vec{E}_0 e^{-i(\vec{k}\cdot\vec{r})} \cdot \vec{E}_n^*(\vec{r}) + \vec{E}_0^* e^{i(\vec{k}\cdot\vec{r})} \cdot \vec{E}_n(\vec{r}). \quad 4.2$$

The $\left|\vec{E}\right|^2$ terms of Eq. 4.2 are referred to as intensity terms, as the same signal would still be present in the absence of other optical fields, whereas the other terms are called interferometric terms. Note that the interferometric terms are here proportional to the optical field. Thus, the aim of phase microscopy techniques is to suppress the intensity terms such that the information in the interferometric terms can be quantified.

Nowadays, there exists several strategies to suppress the intensity terms of Eq. 4.2. The strategies used to quantify the full optical field can approximately be divided into three classes using either: (i) several shifted images, (ii) an off-axis holography configuration, or (iii) deep-learning to recover the phase information in out-of-focus images [15,70,71].

In the case of using several shifted images, which here includes I) phase-shifting [72], II) the transport of intensity equation [70] and III) spatial light interference microscopy [73], a set of images with a known difference between them are used to obtain the optical field. The working principle of the phase-shifting approach is the following: if one of the optical fields in Eq. 4.2 is phase shifted, the intensity terms remain the same while the contribution from the interferometric terms changes. In particular, if the phase shift is π, the interferometric terms change sign. Thus, subtraction of images with and without phase-shifting one of the optical fields supresses the intensity terms while still maintaining the interferometric terms [15]. The foundation of the transport of intensity equation is however slightly different. In this case, intensity images from two adjacent planes orthogonal to the optical axis are combined with the propagation equations (see Sections 2.1-2.2) to estimate the optical field. Nevertheless, the principle of having images with a known difference between them remains the same. The benefits of using several shifted images are high optical resolution and that light sources with a short coherence length† can be used. However, this approach has the disadvantage that several images are required, and that the sample

* Coherent optical fields means that the frequency and waveform are identical and the phase difference is constant. Although incoherent optical fields also interfere at any given moment in time, since the phase difference varies much faster than the exposure time of a camera, the recorded interference signal for incoherent field is zero.

† When two initially coherent optical fields travel different distances before recombined at a camera, the fields can become incoherent. The distance difference for which the fields become incoherent is referred to as the coherence length, which is around a few μm for LEDs and can be up to several km for stabilised lasers.

needs to remain unchanged during the imaging cycle. Thus, this approach is limited to stationary or slowly changing experimental systems.

Off-axis holography is instead based on using an external reference beam which is slightly tilted with respect to the light that interacts with the sample (see Figure 9). The tilted external reference beam enables the optical field to be quantified in a single image [15]. This method is presented in detail in Section 4.1.1, as it is the main experimental method used in Paper I. Off-axis holography has the advantage that the optical field is quantified using only a single image, which enables imaging of non-stationary experimental systems. In contrast, it has the disadvantage that a light source with a long coherence length is needed, which makes it prone to coherence speckle noise [74].

The last approach takes advantage of deep learning to recover the phase information from out-of-focus images [71]. In principle, a deep learning algorithm is trained to suppress the unwanted terms of Eq. 4.2, often using training data from approaches (i) or (ii). This combines the benefits of using a single image and light sources with a short coherence length. The method's current drawbacks are that the sample needs to be imaged significantly out-of-focus and that a representative training set is needed to train the algorithm. However, since the method is continuously being developed, it remains to be seen to which extent these limitations will be possible to overcome.

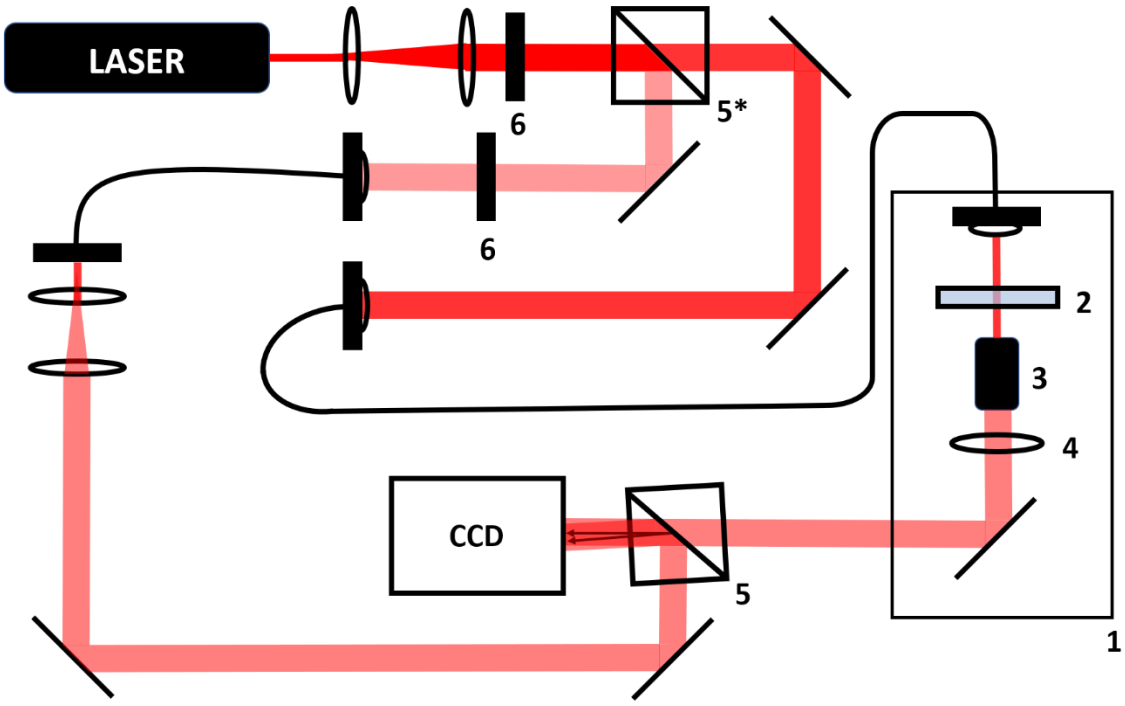

Figure 9: Schematic illustration of an off-axis holographic microscope. The laser beam is split into two different beams, where one passes through the sample and one does not. The two beams are then recombined at the camera with a slight angle with respect to each other. 1. Inverted microscope, 2. Sample, 3. Objective, 4. Tube lens, 5. Beam splitter, 5*. Polarisation-dependent beam-splitter 6.Half-wave plates.

4.1.1 Optical off-axis holographic microscopy

Off-axis holography is a microscopy technique that measures the change of the incoming field induced by a sample, and this using a single image without any assumptions of the sample shape [15]. The technique was first developed in the 1960s by Emmett Leith to overcome some of the issues with Gabor holography, another holography technique developed in 1948 by Dennis Gabor* [75,76]. In Gabor holography, it is difficult to separate the different interferometric terms and the technique is limited to relatively simple objects which transmit a large proportion of the light without scattering [76]. To overcome these limitations, Leith introduced a tilted external reference beam (see Figure 9 and Figure 10), which enabled a straight forward procedure to separate the interferometric terms (see Section 4.1.1).

To motive the use of a tilted external reference beam, we return to Eq. 4.2. If all the optical fields have the same polarisation and the camera plane is defined such that $z = 0$, the recorded image is proportional to:

$$I_{\mathrm{cam}} \propto \left|\vec{E}_0\right|^2 + \left|\vec{E}_n(\vec{r})\right|^2 + E_0 E^*_{\mathrm{obj}}(\vec{r}) e^{-i(\Delta k_x x + \Delta k_y y)} + E^*_0 E_{\mathrm{obj}}(\vec{r}) e^{i(\Delta k_x x + \Delta k_y y)}, \qquad 4.3$$

where $\vec{E}_{\mathrm{obj}}(\vec{r})$ is the light which has interacted with the sample while Δk_x and Δk_y depend on the angle between the external reference beam and the direction of $\vec{E}_{\mathrm{obj}}(\vec{r})$. At this point, it is important to recall the relation $\boldsymbol{\mathcal{F}}(f(x)e^{ik_x x}) = \hat{f}(k - k_x)$, where $\hat{f}(k) = \boldsymbol{\mathcal{F}}(f(x))$ and $\boldsymbol{\mathcal{F}}()$ is the Fourier transform operator for the function inside the parenthesis [37]. Specifically, the multiplication with $e^{-i(k_x x + k_y y)}$ becomes an offset in the spatial frequency space. Thus, the interferometric terms and the intensity terms become separated when the image is Fourier transformed. An example of $\boldsymbol{\mathcal{F}}(I_{\mathrm{cam}})$ is shown in Figure 10. The central peak corresponds to the intensity terms and the off-centre peaks correspond to the interferometric terms. One of the interferometric terms can then be selected by applying a Fourier filter which supresses the other two peaks. The image analysis method to select one of the interferometric terms is standardised and outlined in several scientific articles; thus for extensive details see Kim [15]. In brief, by centring one of the off-centre peaks, multiplying with a circular selection Fourier filter and then applying an inverse Fourier-transforming the filtered image, the optical field is obtained (see Figure 10) [15]. Thus, the tilted external reference beam allows for a numerical procedure to separate the intensity and interferometric terms using only a single image.

Once the optical field is obtained, the phase information can be obtained using the argument of the complex numbers. The advantage of using off-axis holography to quantify the induced phase shift is that it is relatively unsensitive to light attenuation

* Holographic microscopy was initially developed for electron microscopy, but it was quickly realised that the same principles could be used in optical microscopy.

from the sample, whereas ordinary phase microscopy methods assume the sample only affects the phase of the incident light [15]. Furthermore, by utilizing the propagation algorithms in Sections 2.1-2.2, the optical field can be repropagated and analysed at any arbitrary z-plane, enabling analysis of particles throughout the sample volume. For this reason, off-axis holography has been extensively used in various cell studies [15,16,43]. This aspect of off-axis holography was utilized in Paper I to enable particle tracking throughout the volume of a microfluidic channel.

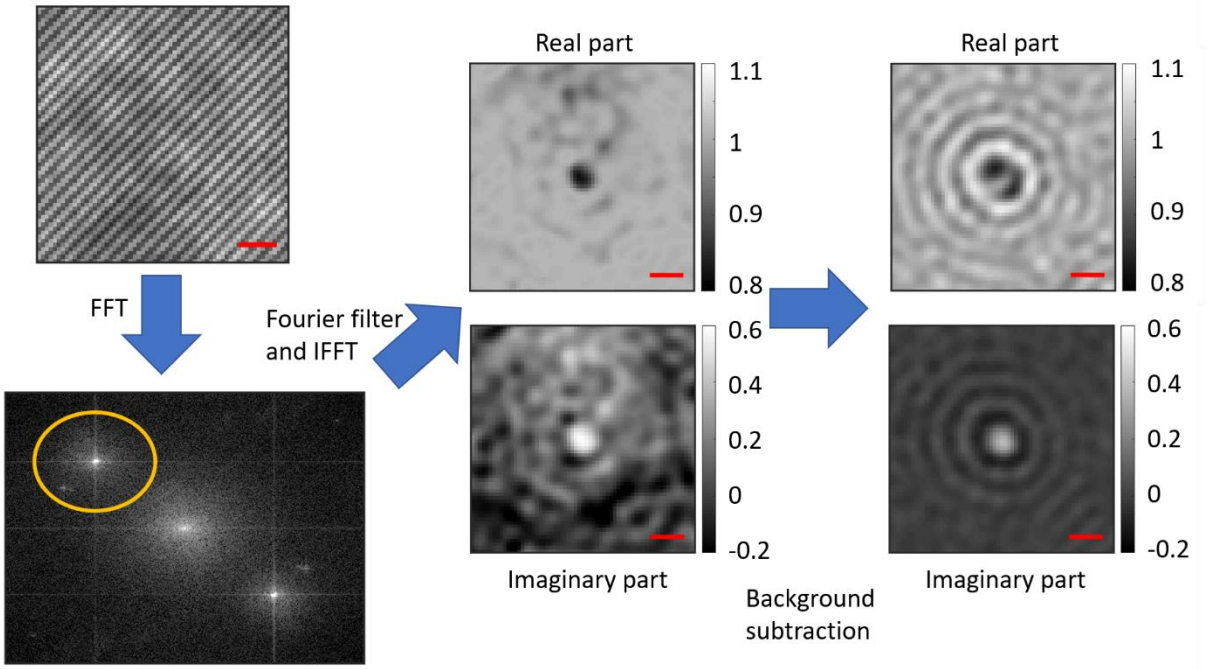

Figure 10: Illustration of the initial data processing steps of the off-axis holography data. All images with a scalebar correspond to the same region in the sample, the only difference is the amount of data processing. The recorded image at the camera is Fourier filtered such that the optical field is obtained. The optical field is then normalised such that the plane-wave background is equal to 1. The stationary background signal is thereafter subtracted. The scalebars correspond to 1 µm.

4.1.2 Characterisation of subwavelength particles using their optical signal

By using the theory developed to represent the optical signal from small particles (see Section 2.4), the optical scattering pattern from a known particle can be calculated. Thus, if the objects in the sample are known, then the corresponding microscopy image is also known except for experimental noise and optical aberrations. However, in the vast majority of measurements, the particles are unknown and the goal is to describe the particles based on their corresponding microscopy image. Without any previous knowledge about the particles, finding a unique solution is a very challenging problem, particularly due to the limited spatial resolution of optical microscopy. This problem is often referred to as the inverse problem, whereas calculating the signal from known particles is called the direct problem [30].

For this reason, if the particle shape is unknown, either the shape needs to be assumed or the signals are being quantified without any reference to particle size or shape. The advantage of assuming particle shape is that it allows to quantify particle size directly from an image using the spatial distribution of the signal [21]. Since the signal amplitude is approximately the product of particle volume and the refractive index difference between the particle and the surrounding medium, the refractive index of the particle can also be obtained once particle size is known [17,21]. When assuming particle shape, a spherical approximation is often used [18]. This enables fitting using Mie theory (see Section 2.4) with the radius and refractive index as free parameters. If the particle deviates from a sphere, the signal can often be replicated by an effective sphere, in particular if the particle size is smaller than the point spread function (PSF) of the measurement [20,77], where the PSF contains the effect of the wavelength, optical aberrations, distance from the focal plane, and numerical aperture of the objective [78]. However, the estimated radius and refractive index should then be referred to as *effective* fitting parameters. Nevertheless, depending on the *a priori* information about the measured particle system, the effective parameters can be related to physical particle parameters. For example, for elongated particles, the relation between effective radius and refractive index contains information about particle orientation [79], and for particle clusters the effective radius and refractive index relate to the fractal dimension and the number of monomers in the cluster [17,20].

However, one limitation of the Mie fitting approach is that it becomes unreliable for nanoscopic particles, which is a consequence of the optical spatial resolution limit and noise in experimental images [21]. Specifically, as the particle size decreases, the spatial distribution of the signal becomes dominated by the properties of the microscope, as for example the wavelength and optical aberrations [80]. Since the size determination using Mie theory depends on the spatial distribution of the optical signal, pushing the limit of the particle sizes which accurately can be quantified using Mie fitting depends partially on the ability to correct for such aberrations. For example, Mie fitting still works for simulated nanoparticles in noise-free images [81]. Corrections of the induced effect of the microscope can be performed by taking into account that the measured signal is a convolution between the particle signal and the PSF [78]. To correct for the effect of aberrations, the strategy used in Paper I was to perform calibration measurements using monodisperse particles with a known size and refractive index. Specifically, by comparing calibration data with theory and taking advantage of the mathematical theorem that a convolution becomes a multiplication when Fourier transformed [37], the experimental PSF and its spatial variations could be estimated.

As indicated in the previous paragraph, there is a lower size limit below which the simultaneous determination of both size and refractive index from the optical signal becomes unreliable. Nevertheless, the signal amplitude can still accurately be quantified, while other size-dependent information such as the diffusion constant can be combined with the particle signal to determine the refractive index [17]. However, accurate estimation of the radius using the diffusion constant requires several particle

observations as well as knowledge about the viscoelastic properties of the medium and the hydrodynamic boundary conditions; aspects that were discussed in detail in Section 3.4.

4.1.3 Image analysis of holography data using deep learning

Classical image analysis is typically based on using a fixed set of mathematical operations, such as convolutions and thresholds, combined with intuition about the experimental system in question [82]. Despite the historical success of this approach, the obtained solution is not necessarily the optimal for the task at hand. In particular, the explored space of potential solutions[*] is significantly limited, and the solution depends on the knowledge of the user. For images with a high signal-to-noise ratio and distinct features of interest, different image analysis algorithms give similar outcomes. But as the signal-to-noise ratio decreases, which is the case when smaller particles are analysed, the used algorithm may significantly affect the accuracy of the quantified particle parameters [66,83].

An alternative image analysis approach to solve the task at hand is letting a computer find the combination of parameters for the mathematical operations, an approach referred to as machine learning. In essence, machine learning is based on setting up a space of mathematical parameter combinations, in which a computer explores different combinations given a certain set of rules [82]. There exist several different classes of machine learning, both regarding the mathematical operations the algorithm performs and how the end-result is obtained. In the context of quantitative image analysis of microscopy data, convolutional layer-based neural networks trained using supervised learning is commonly used, as they are translation-invariant and requires relatively few free parameters to be optimised [71,82,84]. The structure of the network depends on the considered application. For example, the so called U-NET structure has successfully been applied to holography data to achieve phase recovery, denoising and virtual staining [71,85] among others, whereas convolutional neural networks (CNN) and dense neural networks have been used to quantify size and refractive index from particle scattering patterns [21,86].

There are both advantages and disadvantages of using deep learning-based image analysis compared to classical image analysis. The main disadvantages are that training data is needed, which either is experimentally obtained or simulated, and that the algorithm often needs retraining when transferred to another microscope. Depending on the complexity of the experimental system, the challenge of generating training data varies. However, as outlined in Section 4.1.2, calculating the signal from known particles (the direct problem) is often significantly easier than the inverse problem [30]. Thus, deep learning can this way shift the inverse problem in classical image analysis

[*] The phrasing “space of potential solutions” comes from viewing the task as a multi-dimensional optimisation problem, where each free parameter, such as threshold values, is a separate dimension in the space of potential solutions. Thus, by increasing the number of free parameter and the range of searched values, the space of mathematical parameter combinations becomes larger.

to the direct problem. Furthermore, there are now several open-source software packages available that aid in this step of the analysis [84], thus reducing the complexity for individual users.

There are numerous potential advantages of using deep learning instead of classical image analysis. For example, deep learning-based image analysis opens up for new possibilities such as recovering the phase information from a single out-of-focus image [71] and virtual staining [85]. In Paper I, deep learning was used to enable weighted averaging of a stack of particle observations, such that the averaging became independent on particle centring in the images. The used network structure also generated a weight for each single observation based on noise and image quality to further improve the parameter estimation. Another advantage is improved performance at low signal-to-noise ratios, since neural networks are efficient at separating signals occurring at different length scales, where noise, the signal of small particles, and the background signal often have different spatial correlation. For example, in the case of single-particle tracking, deep learning algorithms have been shown to reduce the uncertainty in position determination and improve particle detection [66,83].

4.2 Two-dimensional flow nanometry

When quantifying the diffusion constant of individual particles, long track lengths are needed to reduce the statistical uncertainty (see Section 3.4). However, if the particles are free to move unrestrictedly in 3D, they will eventually move outside the imaging region, which consequently limits the experimentally obtainable track lengths. To overcome this limitation, one solution is to restrict the motion of the particle by using nano- or microfluidic designs [87,88]. Another approach is to molecularly link the particles to a laterally fluid supported lipid bilayer (SLB), as illustrated in Figure 11, which restricts the particle motion to two dimensions [89]. Although long track lengths can readily be obtained using any of these approaches, the particle mobility is affected by the confinement (see Section 3.2). Furthermore, when a particle is molecularly linked to an SLB, the motion of the particle-tether complex depends also on the mobility of the linker (see Section 3.3) [62,63]. Thus, when using any of these approaches, the ordinary Stokes-Einstein equation cannot be used to relate diffusivity to particle size without first introducing corrections for the particular system under investigation [47].

In the case of nanoparticles tethered to an SLB, one strategy to avoid the added complexity when relating diffusivity to particle size is to introduce a shear flow and use the ratio between the flow-induced velocity and the diffusivity of the particles [63]. Implied by the Einstein–Smoluchowski relation [8], the ratio between the flow-induced velocity, v, of the particle and the diffusion constant, $D_{\mathrm{th-NP}}$, relates to the hydrodynamic force as:

$$F = k_{\mathrm{B}}T\frac{v}{D_{\mathrm{th-NP}}}. \qquad 4.4$$

Assuming spherical particles, F is related to particle size, R_{FN}, as: [63]

$$F = k_{\mathrm{B}}T\frac{v}{D_{\mathrm{th-NP}}} \approx A\eta u_0 R_{\mathrm{FN}}\left(R_{\mathrm{FN}} + \tilde{\lambda}\right), \qquad 4.5$$

where u_0 is the flow rate of the surrounding fluid, η the dynamic viscosity of the surrounding fluid, while A and $\tilde{\lambda}$ are calibration parameters which depend on the experimental geometry and hydrodynamical boundary conditions. In other words, since both the flow-induced velocity and the diffusion constant depend on the mobility of the tethered particle, their ratio cancels the effect from the unknown mobility. This approach to measure particle size is called two-dimensional flow nanometry (2DFN) and is the main experimental imaging technique in Paper II. The advantage of 2DFN is that it enables simultaneous quantification of both the size and diffusion constant without requiring a known relation between the optical signal and size. However, the main disadvantage with 2DFN is that it requires tethering of particles to a fluid interface, which limits the type of particles that can be analysed.

When relating measured particle properties, such as diffusion constant or fluorescence intensity, to R_{FN}, it is important to consider the physical meaning of R_{FN}. In Paper II and in previous work using 2DFN [63,90], the calibration was done by relating the measured hydrodynamic force distribution to the hydrodynamic size distribution obtained using bulk-based nanoparticle tracking analysis (NTA). This makes R_{FN} similar to the hydrodynamic radius but not necessarily identical. If the particles used during calibration have a non-zero size distribution, there might be a difference between the measured particle size distribution in 2DFN and in bulk. This introduces a potential bias in size determination using 2DFN. A detailed investigation of this effect is presented in the supplementary information to Paper II.

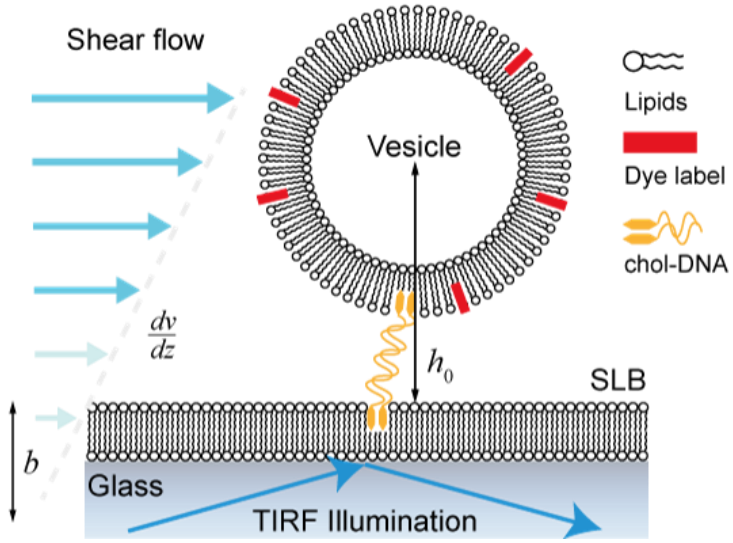

Figure 11: Schematic of a two-dimensional flow nanometry (2DFN) measurement. Particles (here a lipid vesicle) are linked to a supported lipid bilayer (SLB) using molecular tethers, here a cholesterol-DNA tether. A shear-flow is applied such that the tethered vesicle has a non-zero drift velocity. The particles are here imaged using fluorescence microscopy.

4.2.1 Limitations of two-dimensional flow nanometry

When applying Eq. 4.5 to estimate particle size, it is implicitly assumed that the velocity of the fluid around the particle is considerably faster than the velocity of the SLB. To illustrate this approximation, it is instructive to inspect the Langevin equation of motion (see Section 3). If the flow direction is along the x-axis, then the equations of motion are:

$$m\frac{dv_{\mathrm{x}}}{dt} = -\mu_{\mathrm{NP}}^{-1}(v_x - v_{\mathrm{fluid}}) - \mu_{\mathrm{T}}^{-1}\,(v_{\mathrm{x}} - v_{\mathrm{SLB}}) + \xi_x(t) \qquad 4.6$$

$$m\frac{dv_{\mathrm{y}}}{dt} = -\mu_{\mathrm{NP}}^{-1}v_{\mathrm{y}} - \mu_{\mathrm{T}}^{-1}v_{\mathrm{y}} + \xi_{\mathrm{y}}(t) \qquad 4.7$$

where μ_{NP} is the nanoparticle mobility, μ_{T} is the mobility of tether(s) in the SLB and $\xi(t)$ is the stochastic force (see Section 3). Since the velocity of the fluid is different for different parts of the particle, v_{fluid} here refers to the average velocity of the fluid interacting with the particle, which is assumed to be identical to the fluid velocity at the height corresponding to the centre of the particle [63].

Equation 4.7 is similar to the ordinary equation for Brownian motion. Thus, the diffusion constant along the y-axis is given by $D_{\mathrm{y}} = k_{\mathrm{B}}T/(\mu_{\mathrm{NP}}^{-1} + \mu_{\mathrm{T}}^{-1})$. Furthermore, when a particle has reached its steady-state drift velocity, $<\frac{\mathrm{d}v_{\mathrm{x}}}{\mathrm{d}t}>= 0$, Eq. 4.6 gives:

$$\mu_{\mathrm{NP}}^{-1}v_{\mathrm{fluid}} + \mu_{\mathrm{SLB}}^{-1}v_{\mathrm{T}} = v_{\mathrm{x}}(\mu_{\mathrm{NP}}^{-1} + \mu_{\mathrm{T}}^{-1}) \;=\; k_{\mathrm{B}}T\frac{v_{\mathrm{x}}}{D_{\mathrm{y}}}. \qquad 4.8$$

Furthermore, the particle mobility is defined as the ratio between the terminal drift velocity and the applied force, $\mu = v/F$. Thus, $\mu_{\mathrm{NP}}^{-1}v_{\mathrm{fluid}}$ is the hydrodynamic force in Eq. 4.4. Therefore, to obtain Eq. 4.4 from Eq. 4.8, it is required that $\mu_{\mathrm{NP}}^{-1}v_{\mathrm{fluid}} \gg \mu_{\mathrm{T}}^{-1}v_{\mathrm{SLB}}$. Measurements of v_{SLB} show that its velocity is over a factor 100 lower than the fluid velocity at the height of a 50 nm radius particle [91]. Furthermore, the results from Paper II show that μ_{NP}^{-1} is similar to μ_{T}^{-1} in the case of a single tether and a 50 nm radius particle. However, since both μ_{NP}^{-1} and the distance from centre of the particle to the SLB decrease with reducing particle size, there is a lower size limit at which this approximation is no longer valid. The lower particle size limit for when 2DFN can be accurately applied is around 10-20 nm (in diameter) [63].

Furthermore, to obtain the relation $F \approx A\eta u_0 R_{\mathrm{FN}}\left(R_{\mathrm{FN}} + \tilde{\lambda}\right)$ given in Eq. 4.5, it is implicitly assumed that $\mu_{\mathrm{NP}}^{-1} \propto R$ [63]. However, as discussed in Section 3.2, the diffusivity-size relation deviates from the ordinary Stokes-Einstein relation when the particles are in close proximity to the surface. Since $\mu = Dk_{\mathrm{B}}T$, this also holds for the particle mobility. Thus, Eq. 4.5 should be viewed as an approximate relation. This is of importance since $\tilde{\lambda}$ is sometimes referred to as the slip length (see Section 3.1). Although $\tilde{\lambda}$ to some extent is dependent on the slip length, due to the approximations when deriving the expression, there are several other contributions to its numerical value, such as confinement effects and the finite viscosity of the SLB [11,13]. Thus, to

quantify the slip length using 2DFN, the size-diffusivity data needs to be evaluated using Eqs. 3.8-3.10, which was inspected in detail in Paper II.

Another central assumption when using 2DFN is that the particle mobility is the same throughout the measurement. If the tethering is multivalent, as in the case for Paper II, the number of tethers may change during the trace [64]. This complication can be handled either by evaluating the diffusion constant using a sliding window approach, which checks if it is the same throughout the trace, or by comparing the diffusion constants parallel and orthogonal to the flow direction. In the latter approach, if the number of tethers change, then the mean step length in the flow direction becomes incorrect, which makes the diffusion constants deviate from one another. This second approach was used in Paper II to only include particles for which the number of tethers is constant during the track and did not interact with potential defects in the SLB.

4.2.2 Total internal reflection fluorescence microscopy

As indicated in Section 2.5, by using wavelength-selective filters it is possible to separate a fluorescence signal from the incoming illumination. The main differences between the many existing fluorescence microscopy methods arise from the size of the illumination volume and how the molecules are excited. For example, in epifluorescence microscopy, the sample is illumined by a stationary light beam, whereas in confocal fluorescence microscopy a small optical probe is scanned over the sample, where in both cases either single and double photon excitation are commonly used [44].

If the objects of interest are in close proximity to a surface, it is possible to use the evanescent field from total internal reflection to only excite particles in vicinity to the surface (see Figure 12). Total internal reflection is a phenomenon which occurs when a ray of light interacts with a medium with lower refractive index and the angle relative to the normal direction of the surface is larger than a critical value determined by the ratio of the two refractive indices. When this happens, there is no direction in the second medium in which constructive optical interference in the far field* can occur. Instead, the light reflects at the surface. However, although the far field is zero, there is still a non-zero optical near field, here called the evanescent field, which exists close the interface between the two media.

The evanescent field decays exponentially, $I = I_0 \mathrm{e}^{-z/\delta}$, with the characteristic length δ,

$$\delta^{-1} = \frac{4\pi}{\lambda}\sqrt{(n_1 \sin\theta)^2 - n_2^2}, \qquad 4.9$$

* The far field is the signal which can be captured by an ordinary camera, whereas the near field is the part of the optical field which cannot. Nevertheless, the near field is important for close range interaction, as in the case of an evanescent field.

where n_1 is the refractive index of the original medium, n_2 is the refractive index of second medium and θ is the relative angle between the incoming ray of light and the normal of the surface [22,32]. Fluorescence microscopy which uses this type of excitation illumination is called total internal reflection fluorescence (TIRF) microscopy. TIRF is commonly used when analysing particles attached to an SLB as it suppress the potential background signal from particles in bulk [92–94], a feature used in Paper II.

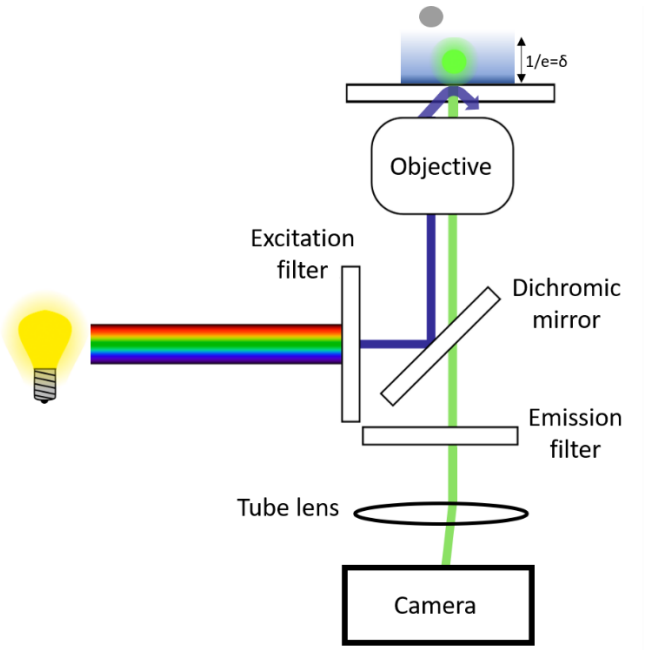

Figure 12: Schematic illustration of a total internal reflection fluorescence (TIRF) microscope. The incoming light is wavelength filtered to match the absorption spectrum of the fluorophores. The incoming light approaches the sample with an angle such that total internal reflection occurs, which gives rise to an exponentially decaying evanescent field which excites the fluorophores close to the surface. δ is the characteristic length constant for the exponentially decaying evanescent field. The subsequent emission is wavelength filtered and recorded by a camera. The image is adapted from Wikimedia [95] under CC BY-SA 1.0 licence.

4.3 Comparison between optical holography and different microscopy characterisation techniques to estimate particle size

Although both holographic microscopy and fluorescence microscopy combined with 2DFN are used to quantify particle size in Paper I and II respectively, the size is extracted directly from the images only when using holographic microscopy. The reason for the difference in size quantification between the methods does not only relate to the different particle sizes used in the respective investigations, it also relates to differences between fluorescence and optical scattering. For example, the fluorescence signals from different parts of a particle are incoherent with each other, where the coherence aspect of optical scattering contains a significant amount of the size information (see Section 2.4). For this reason, the size determination approach used in Paper I is difficult to apply for fluorescence data. Another difference is that the fluorescence intensity depends on both exposure time and the chemical environment around the fluorophores, which implies that the signal amplitude does not necessarily scale with particle volume [90,96]. Thus, it is challenging to quantify the size of subwavelength particles using the amplitude and spatial distribution of the fluorescence signal. Nevertheless, fluorescence is a specific signal whereas scattering originates from all refractive index inhomogeneities (see Sections 2.4-2.5), and specificity is advantageous when investigating the motion of weakly optically scattering objects such as lipid vesicles.

Regarding the use of off-axis holography in Paper I, there are several different interferometric/scattering techniques that are capable of quantifying both size and refractive index of individual particles. One such technique is flow-cytometry, which has been used to measure the size of lipid vesicles by quantifying the angular scattering pattern [19]. Another technique is dark-field optical microscopy combined with particle tracking, which is based on that the scattering intensity and hydrodynamic radius can be used to estimate the refractive index (see Section 2.4) [97]. A third technique is in-line holography, in which Mie fitting is applied to out-of-focus microscopy images [18]. The particle sizes that can be analysed using flow-cytometry and dark-field microscopy are considerably smaller than the sizes that can be observed using off-axis holography. One major reason for this difference is that optical holography is a brightfield technique whereas flow-cytometry and dark-field NTA are dark-field techniques. In the limit of small particle sizes, the signal-to-background ratio becomes critical. Off-axis holography can also be used in a dark-field configuration [98], but then the signal contains no information about the phase-shift induced by the particle since that requires information about the phase of the incident light.

However, dark-field techniques also have disadvantages. For example, they struggle with simultaneous size-refractive index determination for particle sizes comparable to or larger than the wavelength of light. This originates from that the scattering signal does not monotonically increase with particle size, with the size interval within which the signal monotonically increases being dependent on the illumination

geometry [97,98]. Ordinary off-axis holography does not have that issue since the integrated phase scales monotonically with particle volume [17]. Thus, the performance of the different scattering/interferometric techniques varies depending on the size-interval in question, where holography is preferable for particles larger than the wavelength of light and dark-field techniques are currently preferable for nanoparticles.

Furthermore, it is difficult with flow cytometry and dark-field NTA to investigate dynamical changes on the single-particle level. Flow cytometry only takes a snapshot of the particle in question, whereas diffusion-based sizing requires that changes in particle size occurs on a time scale much slower than the imaging frame rate (see Section 3.4). Thus, for experimental systems where it is of interest to follow changes for the same particle over time, holographic microscopy is advantageous. However, other holographic microscopy methods such as in-line holography can also be used to quantify dynamics on the individual particle level. One major difference between in-line holography and off-axis holography is that in-line holography requires the particle to be imaged considerably out of focus, whereas off-axis holography can handle both in and out-of-focus particles. This limitation of in-line holography is one of the reasons why the minimum particle radius to accurately determine both size and refractive index is around 500 nm [86,99]. Thus, for particles with a radius larger than 500 nm both in-line and off-axis holography can be used, but for subwavelength sized particles only off-axis holography has so far been able to experimentally quantify size and refractive index.

5

Summary of results

"Because I enjoy it."
Michelson's answer to Einstein's question regarding why he spent so much effort on measuring the physical constants. [100]

This chapter summarises the two papers that this thesis is based upon, referred to as Paper I and Paper II. Paper I is focused on quantifying size and refractive index of subwavelength sized particles using the optical scattering pattern measured with off-axis holography, and where deep-learning was used to improve the parameter determination. The developed method was used to quantify size and refractive index of individual particles in dispersions with different solution properties as well as to resolve reversible fluctuations of the number of monomers for polystyrene nanoparticles clusters. Paper II is focused on the quantification of hydrodynamic boundary conditions using two-dimensional flow nanometry (2DFN, see Section 4.2) for nanoparticles tethered to a supported lipid bilayer (SLB). The experimentally obtained size-diffusivity relation was evaluated against theoretical expressions to quantify the slip length for two different lipid vesicles, as well as to clarify the size-dependent mechanistic aspects concerning the mobility of membrane-attached nanoparticles. For details beyond the summaries in the following sections, see the Papers appended to this thesis.

5.1 Paper I

This investigation is based upon developing an alternative to the Stokes-Einstein relation when using optical microscopy to quantify size of subwavelength sized particles, as such sizing cannot be applied for dynamically changing particles or for particles in unknown surrounding media. One alternative approach to quantify both the size and refractive index without the limitations of the diffusivity-size relation is to fit the optical scattering pattern to simulations of known particles (see Section 4.1.2). Previous implementations of this approach, however, either struggle with subwavelength sized dielectric particles or cannot follow the same particle over time [18,19,99].

To develop a method which partially overcomes these limitations, off-axis holographic nanoparticle tracking analysis (H-NTA) was combined with a deep learning-based analysis called weighted average convolutional neural network (WAC-NET) to characterise both the size and refractive index using the optical scattering pattern. The WAC-NET was trained using Mie simulations combined with noise to mimic the experimental data. The performance was subsequently evaluated using experimental data of particles with known size and refractive index.

For polystyrene (PS) particles which according to the manufacturer had a radius of 228 ± 6.8 nm, the WAC-NET analysis provided estimates on the single particle level for both the radius and refractive index with standard deviations (std) of ±16 nm and ±0.05 refractive index units (RIU) using only five particle observations. By increasing the number of observations to 60, the std became ±11.9 nm and ±0.03 RIU, showing that the output converges using only a few particle observations.

To further evaluate the performance, a mixture of 210 nm radius silica (SiO_2), 150 nm and 230 nm radius PS particles in water were analysed and correctly identified (see Figure 13(a)). Thus, the method can handle mixed samples with particles of different sizes and refractive indices. When changing the viscosity and refractive index of the surrounding medium, the WAC-NET analysis correctly estimated the size and the difference in refractive index between the particle and the media, even though the training data only contains simulations of particles in water. Thus, the characterisation does not require a known surrounding medium.

To test the network in a dynamic scenario, a sample consisting of a solution of 31 nm radius PS nanoparticles was analysed during salt-induced clustering. Since these aggregates are not homogenous spheres, the quantified size and refractive index are effective particle parameters, but these effective parameters can in turn be related to the number of monomers and the fractal dimension[*] of the cluster [20]. The obtained fractal dimension of 2.35 ± 0.1 agrees well with the expected fractal dimension considering that diffusion-limited clustering of monodisperse monomers have a fractal dimension of ~2.5 and the fractal dimension decreases if cluster−cluster aggregation occurs [101]. Further, as seen in Figure 13(b), the size and refractive index change over time while the fractal dimension is approximately constant, demonstrating that the clustering process is dynamic and has a reversible nature.

In conclusion, this work shows that the size and refractive index can accurately be measured for dielectric particles with a minimum radius of $\sim$150 nm using only a few particle observations. Compared to diffusivity-based sizing, the WAC-NET analysis requires approximately a factor of 100 fewer observations to achieve the same accuracy for individual particles. As the characterisation is performed without assumptions on

[*] Fractal dimension D_f is here referred to as the scaling between the size and the number of monomers, N, where $r^{D_f} \propto N$. Pictorial depictions of possible clusters for three different fractal dimension are shown in Figure 13(b).

the physical properties of the environment and shape of the particle, it can be applied for a wide range of experimental systems as long as the particles generate a large enough optical signal. In particular, the characterisation is sufficiently accurate to provide a reliable time-resolved estimate of the fractal dimension of individual aggregates, which, to our knowledge, has not previously been reported.

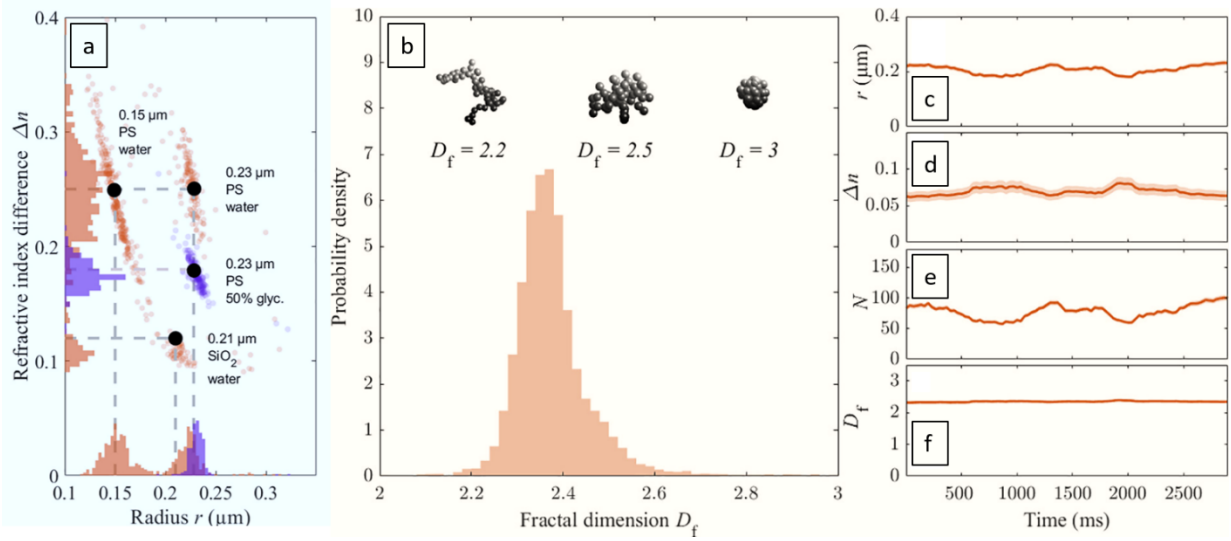

Figure 13: Summary of the main results in Paper I. (a) The WAC-NET approach (using 60 observations) distinguishes and correctly characterises subpopulations in a multicomponent mixture dispersed in water, consisting of 0.21 µm silica (SiO_2), 0.15 µm polystyrene (PS), and 0.23 µm PS particles. Furthermore, it also correctly characterises size and the refractive index difference Δn of 0.23 µm PS particles dispersed in a 50% glycerol/water mixture. The intersections of the dashed lines represent the expected positions of the populations. (b) The WAC-NET approach gives an average fractal dimension D_f close to 2.35 for salt-induced clustering for 31 nm radius PS nanoparticles. The insets show some pictorial depictions of possible clusters for three different fractal dimensions. (c–f) Time-resolved behaviour of a representative cluster, characterised in terms of its radius r (c), refractive index difference Δn (d), number of monomers N (e), and fractal dimension D_f (f). While r, Δn, and N greatly vary over time, D_f remains stable. The shaded regions represent the estimated standard deviation of the error. The cluster is characterised using a moving window of 20 observations, acquired at a frame rate of 30 frames per second. Adapted from [21] under CC-BY license.

5.2 Paper II

This investigation is based around two current limitations regarding relating nanoparticle diffusion to properties of the experimental system. First, when relating nanoparticle diffusivity to size, the no-slip boundary condition is commonly assumed. However, this assumption cannot be derived from first principles. Furthermore, there are substantial experimental evidence showing deviations from no-slip for several different surfaces, but direct evaluation of partial slip for nanoparticles is difficult using existing methods [12,23,25]. Second, when partial slip occurs, the equations describing confined nanoparticle diffusion close to a planar surface are uncertain when the slip-length is similar to the distance from the surface [13,56]. Thus, there is a need for new approaches to experimentally quantify the hydrodynamic boundary conditions for nanoparticle systems in general, and mobility of nanoparticles close to a surface with partial slip in particular. Furthermore, considering that a distance similar to the potential slip-length is naturally present during the initial interaction between biological nanoparticles and cellular membranes [102], clarifying the size-dependent mechanistic aspects concerning the mobility of lipid bilayer attached nanoparticles is also of biological relevance.

To investigate these questions in the context of biological nanoparticles close to an SLB, 2DFN was used to simultaneously measure particle size and diffusivity of both POPC lipid vesicles and extracellular vesicles (EVs). The vesicles were tethered using cholesterol-DNA tethers to an SLB formed on the glass floor of a rectangular PDMS microfluidic channel such that the flow-induced motion of these vesicles could be measured with total internal reflection fluorescence (TIRF) microscopy [63,89]. For a schematic illustration of the experimental system, see Figure 14(a).

From the 2DFN measurement, when inspecting the flow-induced velocity and the diffusivity (see Figure 14(b)), the data is not continuously distributed but is instead gathered in clusters. This data clustering is caused by the fact that vesicles can be tethered with more than a single tether. Thus, within each cluster only particle size varies. Since both size, diffusivity and number of tethers are known for vesicles within a particular tether subpopulation, this opens up a possibility to fit the measured size-diffusivity relation using the slip lengths b as fitting parameters.

When deriving the size-diffusivity expression under the assumption of short slip lengths, $b \ll R$, the distance between the nanoparticle and the SLB, δ, the slip length at the SLB interface, b_{i}, and the slip length at the vesicles, b_{p}, enter the expression as a sum. Thus, the size-diffusivity relation has two fitting parameters, defined as $b_{\mathrm{ef}} \equiv \delta + b_{\mathrm{i}} + b_{\mathrm{p}}$ and D_{T}, where D_{T} is the diffusivity for a tether without any vesicle. A fit of the POPC data in Figure 14(c) results in $b_{\mathrm{ef}} = 22.8 \pm 6.3$ nm and $D_{\mathrm{T}} = 2.56 \pm 0.07$ $\mu m^2/s$. The obtained D_{T} is similar to complementary tether diffusivity measurements using fluorescence recovery after photobleaching (FRAP) of labelled DNA-cholesterol

tethers, suggesting that the separate clusters indeed correspond to individual tether subpopulations.

Additional measurements of POPC vesicles in different buffer salt concentrations resulted in a b_{ef} of around 21-26 nm, whereas measurements of the extracellular vesicles (EVs) resulted in a b_{ef} of $\sim$31 nm. These lengths are considerably longer than the height of the PEG2000 in the SLB, which is $\sim$4 nm [103], and the length of the DNA tether, which is $\sim$15 nm, that together set range of potential b_{ef} values if no slip occurs. Since the slip length is expected to be similar for the POPC vesicles and the EVs, the difference in b_{ef} is likely due to the complex membrane composition of EVs, with protruding proteins and hydrocarbons [27] increasing their distance to the SLB. This indicates that the vesicles are pushed down towards the PEG by the shear flow, resulting in a δ of around 4 nm. Assuming the same slip at both the nanoparticle and the SLB gives a slip length for POPC of around 8-11 nm, which is similar to the literature value for DOPC SLBs of 6 ± 0.5 nm that was measured using a surface force apparatus [61], albeit for planar rather than nanoscale interfaces.

In conclusion, this work shows that the nanoparticle contribution to the size-dependent diffusivity of SLB-tethered nanoparticles can be quantified using a single measurement, where comparison with theory enables evaluation of the hydrodynamic boundary conditions. In addition to the slip length estimation, this finding also clarifies the size-dependent mechanistic aspects concerning the mobility of membrane-attached nanoparticles and enables detailed investigations into how nanoparticle mobility varies between different types of biological nanoparticles.

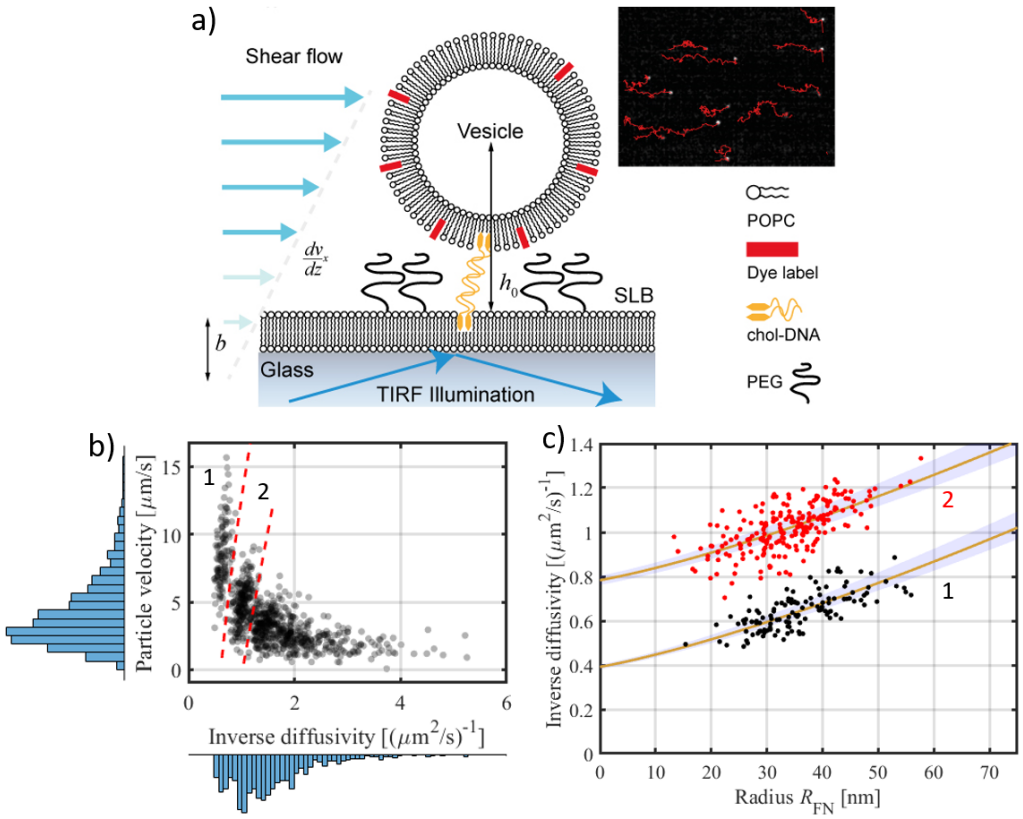

Figure 14: Summary of the main results in Paper II (a) Illustration of the 2DFN concept. Labelled vesicles are linked to a supported lipid bilayer (SLB) using cholesterol-DNA-tethering within a microfluidic channel. A shear-flow is applied and the two-dimensional movement of the vesicles tracked using TIRF microscopy. b indicate the slip length for the SLB and h_0 is the distance from the centre of the particle the SLB. Inset: fluorescence micrograph showing the shearing of vesicles in the field of view with tracks highlighted in red. (b) Flow induced particle velocity versus inverse diffusivity for POPC vesicles tethered to and SLB consisting of POPC. The dashed red lines designate the selection based on the number of tethers (1, 2 and 3+). (c) Inverse diffusivity versus R_{FN} for the first two vesicle-tether clusters in (b). The estimated values from the least-square fit (yellow lines) are $b_{\mathrm{ef}} = 22.8 \pm 6.3$ nm and $D_{\mathrm{T}} = 2.56 \pm 0.07$ μm²/s (mean ± 95% CI, visualized using the shaded blue region).

6

Future outlook

Remember that you are a Black Swan.
– *Nassim Nicholas Taleb*

In the two papers which this thesis is based upon, it is shown that although optical microscopy combined with particle tracking is a well-established experimental technique, there is still room for creative ideas and method improvement. This is particularly true for non-ideal systems in which the ordinary Stokes-Einstein equation cannot be directly applied or when relating the optical signal to particle properties in the 100-500 nm diameter size regime. Although such systems are challenging to investigate, it also offers the potential to experimentally obtain new parameters, as demonstrated in both Paper I and Paper II. Therefore, when looking forward, the main targets are to push the limits of holographic microscopy and to extend the presented investigations to systems of higher complexity.

6.1 Off-axis twilight holography

One of the main limitations with traditional optical holography in the context of measuring nanosized particles originates from the fact that it is a brightfield technique. For brightfield techniques, the background signal tends to dominate the signal from weakly scattering particles, which in turn puts a limit on the weakest signal that can be differentiated from the background. One approach to overcome this limitation is to use dark-field microscopy, in which the illumination pathway is constructed such that the background illumination is not captured by the camera. This approach is used in ordinary nanoparticle tracking analysis (NTA), and has been successfully combined with off-axis holography to improve the limit of detection [98]. However, to quantify the induced phase shift from a particle, which is one of the benefits of using off-axis holography, the background signal is needed. This is so because a phase shift is always relative to the incoming illumination. Thus, dark-field holography is not an ideal solution for quantitative particle analysis.

Although brightfield and dark-field illumination are by far the most common illumination configurations, there is a middle ground between the two which is based

on semi-transparent optical Fourier filters. The working principle of optical Fourier filters is that certain lens configurations perform a Fourier transformation of the incoming optical signal [22,33], which in turn makes is possible to access the spatial frequency information without performing the Fourier transform on a computer. By placing an optical filter in the Fourier plane it is possible to suppress particular spatial frequencies of the optical signal, which in turn shifts the relative signal between different features in an image [104,105].

In the case of plane-wave excitation of a point-like particle, which is the case for off-axis holographic imaging of a nanoparticle, the plane-wave Fourier transforms to a point whereas the optical scattering from the point-like particle Fourier transforms to a plane-wave [37]. Thus, by placing a small optical filter in the Fourier image plane, it is possible to supress the background signal with minor influence on the signal from the point-like scatterer. In particular, by using filters made of thin metallic films, not all the incident light on the filter is removed [104,105]. The reduced but non-zero signal of the incoming illumination enables measurements of the induced phase shift from a particle, where the changed signal-to-background ratio enables weaker optically interacting particles to be measured.

The use of semi-transparent optical filters to improve the signal-to-background ratio is not a new concept when it comes to interferometric microscopy. It was first combined with in-line holography in 2015 under the name of twilight holography [104], and it has later been used in both iSCAT and coherent brightfield (COBRI) microscopy [41,105,106]. However, in these examples the signal amplitude is only a relative signal which needs to be related to a calibration curve. One advantage with off-axis holography is that the phase signal can be directly related to the physical properties of the sample without any calibration curve. When combining off-axis holography with a semi-transparent Fourier-filter, the phase signal changes as the filter affects the relation between the particle signal and the background signal. However, since the optical field is directly obtained in off-axis holography and given that the effect from the Fourier filter is known, it should be possible to compensate for this effect during the data analysis. Thus, off-axis twilight holography can likely improve the detection limit of holography while still maintaining an absolute signal quantification.

In practice, it is difficult to know the exact effect from the Fourier filter in advance. However, it can be estimated by comparing the signal from particles which can be detected both with and without the filter. Although it is difficult to extend the simultaneous size-refractive index quantification presented in Paper I to nanoparticles since a microscope acts as a low-pass filter (see Section 2.3), both the diffusion constant and dynamical changes in the optical signal can still be quantified. Preliminary results for 95 nm and 120 nm radius polystyrene (PS) spheres are displayed in Figure 15. The particle signal is ~2 times larger for the 120 nm radius PS spheres than for the 95 nm PS spheres, which is expected since the particle signal scales approximately with the volume. Thus, these results indicate that it is possible to compensate for the effect of

the filter. For comparison, the smallest PS in Paper I had a radius of 150 nm. Thus, this shows that the size-limit of off-axis holography can be improved well beyond what previously has been reported. The limits of this approach are to be explored in future work, together with applications on biologically relevant nanoparticles, such as lipid nanoparticles and viruses. In particular, by reducing the smallest particle size that can be measured, both aggregation and dissociation of biological nanoparticle clusters should be possible to investigate, which is of importance when it comes to particle stability and inhibition of viruses by attaching particles or large molecules [107].

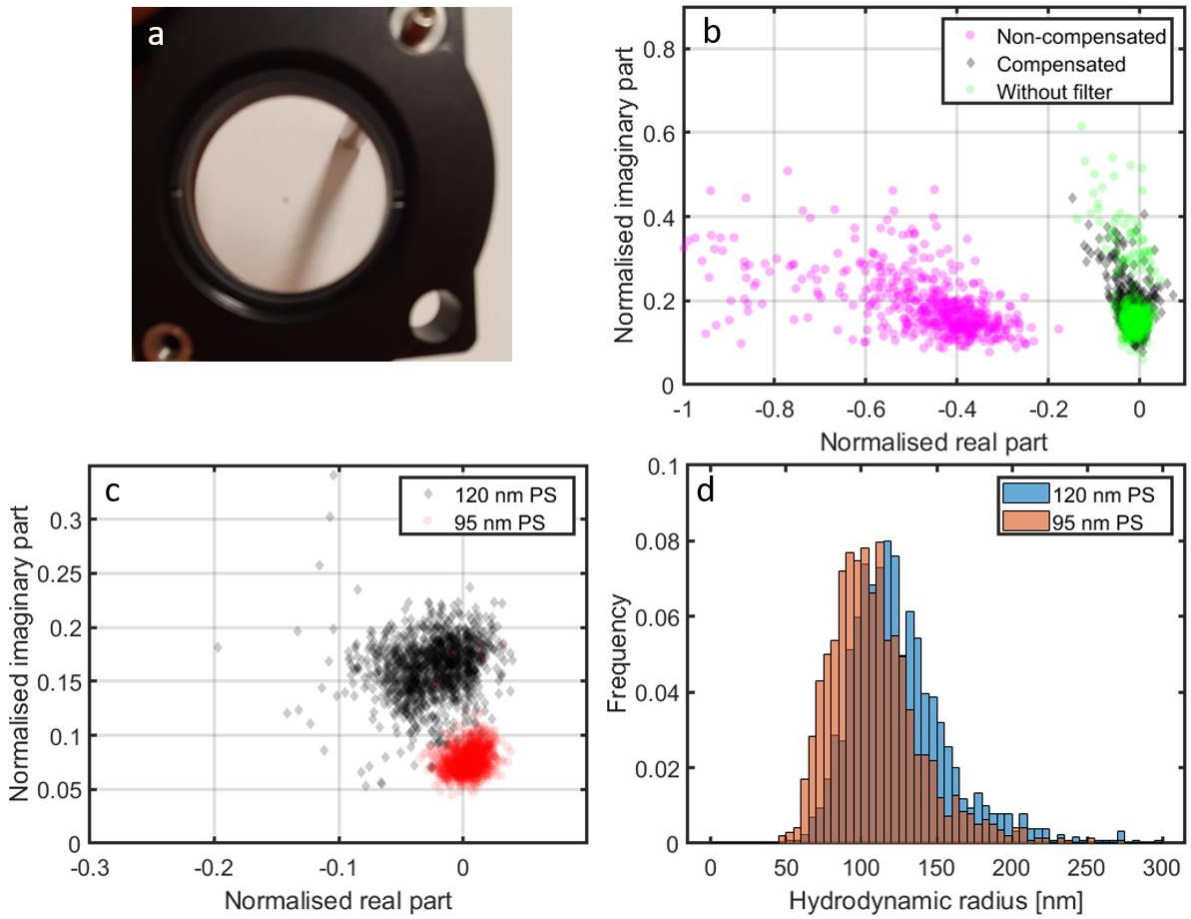

Figure 15: Example of the twilight off-axis holography. (a) The optical Fourier filter is a small gold disc on a glass slide. (b) Measurements of 120 nm radius polystyrene (PS) both with and without the Fourier filter is used to experimentally obtain the effect from the filter. (c)-(d) Measurements of 120 nm and 95 nm radius PS using twilight off-axis holography, where (c) is the measured optical field from the particles and (d) are histograms of the obtained hydrodynamic radius.

6.2 Holographic characterisation of sub-cellular structures using deep learning

When particles interact with for example a living cell, the size-diffusivity relation changes throughout the process and the label-free optical signal becomes dominated by the background of the cell. This makes it difficult to quantify dynamic signal changes using ordinary label-free optical microscopy, especially for subwavelength sized particles. Nevertheless, the particle signal is still present as in Paper I, since it is independent of the complexity of the background signal.

To identify the label-free optical signal of interest in the case of particles inside and/or interacting with cells, the particle identification and background suppression needs to be different than for freely diffusing particles. In the case of small particles inside cells, the particle signal occurs on a shorter length scale than the cell. Thus, one approach is to use various image filters to supress the signal originating from the cell. However, one signal of interest is the integrated phase shift from the particle, where an integration corresponds to a low frequency spatial signal. Furthermore, the signal distribution from a particle depends on its distance from the focal plane. Thus, the signal of interest does not occur on a single spatial length scale. These aspects make it difficult to accurately analyse the corresponding images using classical image analysis.

In Paper I, the particle identification is based on classical image analysis, where deep-learning was only involved in the size-refractive index quantification using the recorded scattering patterns. One alternative image analysis approach is to use deep learning for both particle identification as well as for the signal quantification. In particular, convolutional neural networks have been successfully applied to several different image analysis tasks, where one of its strengths lies in the ability to separate signals which occur at different length scales [82]. When analysing holographic images, one network structure that often is used is the so-called U-NET structure [71,85], in which the output is one or multiple images containing the information of interest. When applied to the task of identifying and quantifying 225 nm radius fluorescently labelled PS particles as well as internal cellular compartments inside SH-SY5Y cells, the U-NET approach works well, as shown in Figure 16. All the visible particles in the phase image as well as those in the fluorescence image are identified by the U-NET, where the U-NET also identifies several non-fluorescent particles, which most likely corresponds to different intracellular compartments. To evaluate the integrated phase shift of the particles in the cell images, it is compared with the quantified phase shift for PS particles measured using holographic nanoparticle tracking (H-NTA) [17]. When only considering the particles that co-localise with a fluorescent signal, the histogram peak is located at a similar position as for H-NTA, showing that the quantification works as intended. The non-fluorescent particles have a different integrated phase distribution than the fluorescent PS particles, further motivating that they correspond to intracellular compartments

The next step is to push the limit of the information which can be extracted from this analysis approach. As both the signal and the 3D-position of every particle is recorded in each image, the U-NET based analysis has the potential of analysing and correlating the signal of a vast number of particles, which would be useful when characterising processes related to for example cellular uptake and internal processing. In particular, since the samples are kept in incubators, it would be of interest to follow the signal changes over time as well as correlating the signal with the particle position in relation to the cell. For example, one interesting question is whether it would be possible to distinguish nanoparticles bound to the outer cellular membrane from particles in side cells, where they are expected to be surrounded by a medium with higher refractive index. Another interesting application is to analyse the dynamic signal of membraneless compartments inside cells, which are of importance when it comes to function of cells but are challenging to investigate using existing methods [108].

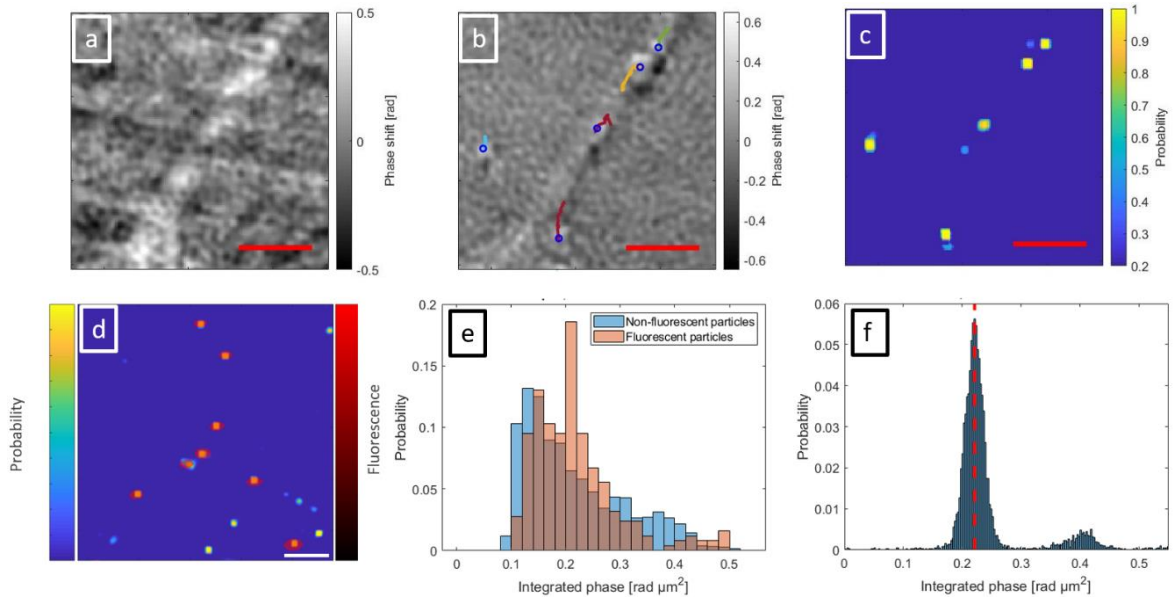

Figure 16: Experimental phase images of subwavelength sized particles both inside and outside cells, and the application of the U-NET on experimental data. (a) A phase image of the area of interest. (b) The same phase image as in (a) is subtracted using a displaced image (where the sample itself have been displaced) to subtract stationary background signal. The image clearly shows the presence of five particles within the field of view, illustrating the benefit of using position modulation to detect dielectric particles inside cells. The traces are the estimated trajectories of the particles (using the output of the U-NET) over approximately 90 seconds, where the motion of the particles follows the layout of the cell, and the motion of each particle inside the cell is mostly in one single direction, indicating directed motion for the particles inside the cell. (c) Image showing the probability output from the U-NET used to identify the particles. (d) Overlay of a probability image and the fluorescence signals, showing that the analysis finds all 225 nm radius polystyrene (PS) particles while also finding several non-fluorescent intracellular compartments. (e)-(f) Histograms of the recorded integrated phase shift, where the similar signal is recorded for the particles in the cell sample in (e) as for the particles measured using H-NTA in (f). The scalebars correspond to 5 micrometres.

6.3 Diffusivity quantification of tethered particles with surface interaction

In Paper II, although the tethering of nanoparticles to a supported lipid bilayer (SLB) and the proximity to the surface makes it deviate considerably from idealised bulk-based nanoparticle measurements, the system is still idealised compared to biological systems. For example, in Paper II there is very little interaction between the nanoparticles and the SLB due to the presence of PEG in the SLB. Thus, after having established the size-diffusivity relation of SLB-tethered nanoparticles during close to idealised conditions, a natural next step is to investigate the effect of a weak interaction between the nanoparticle and the SLB. In particular, tethered nanoparticles could in principle be used to probe weak temporally fluctuating interactions in the limit where it is difficult to quantify the interaction using the residence time of nanoparticle bound to a receptor in an SLB [92]. Another level of complexity is the interaction between tethers when the nanoparticle is multivalently linked to the SLB. In Paper II the main part of the analysis is made using particles which are linked with a single tether to the SLB. As the number of tethers increases, the resulting diffusivity will most likely deviate from independent tether friction contributions to a more collective friction behaviour. Such information would further the understanding of the size-dependent mechanistic aspects concerning the mobility of membrane-attached nanoparticles on native cellular membranes, information that are critical in order to fully understand the initial processes during cellular uptake of nanoparticles.

Acknowledgements

I would like to express my gratitude to everyone which in one way or another has contributed to the development of this thesis.

My main supervisor, Fredrik Höök, I really appreciate that you let me explore and develop my scientific creativity. Thanks for all insightful comments, guidance and the opportunities you provide for me.

My more hands-on co-supervisor, Daniel Midtvedt, I really enjoy our discussions and all the new scientific ideas we continuously develop and explore. It will be interesting to see the final result of all the method development.

My co-supervisor, Elin Esbjörner Winters, and Emelie for always being helpful and bringing such positive energy regarding the cell related aspects of this work, as well as all the suggestions when it comes to applying the developed methods.

My co-authors, both for the papers included in the thesis and those not. Thanks for the good collaboration and that you appreciate my sometimes out of the blue theoretical considerations/ideas. I hope that all the collaborations will continue in the future. A special thanks to Benjamin and Daniel regarding Paper I and Silver, Adrián and Vladimir regarding Paper II, both papers are good examples of when experimental and theoretical insights come together.

I want to thank Excellence Initiative Nano for funding my PhD project and giving me the opportunity to develop my own research ideas.

Past and present members of the Biological Physics group. Thanks for a very open and friendly environment, with very interesting and entertaining discussions during our lunch and fika breaks. A special thanks to my current and past office mates, Mattias, Govindan, Karin and Thomas.

Silver, Adrián, Mattias and Fredrik E, thanks for proofreading this thesis and making it understandable.

I also want to thank Adrián, Mattias, Barbara, Tuve and Alvaro for all the non-work-related activities.

My family and friends, for just being who you all are.

Erik Olsén, Göteborg, April, 2021

References

[1] R. Phillips, J. Kondev, J. Theriot, and H. Garcia, *Physical Biology of the Cell* (Garland Science, 2012).

[2] D. B. Williams and C. B. Carter, *The Transmission Electron Microscope*, in *Transmission Electron Microscopy* (Springer, 1996), pp. 3–17.

[3] Y. F. Dufrêne, *Towards Nanomicrobiology Using Atomic Force Microscopy*, Nat. Rev. Microbiol. **6**, 674 (2008).

[4] P. Török and F.-J. Kao, *Optical Imaging and Microscopy: Techniques and Advanced Systems*, Vol. 87 (Springer, 2007).

[5] R. Brown, *XXVII. A Brief Account of Microscopical Observations Made in the Months of June, July and August 1827, on the Particles Contained in the Pollen of Plants; and on the General Existence of Active Molecules in Organic and Inorganic Bodies*, Philos. Mag. **4**, 161 (1828).

[6] M. D. Haw, *Colloidal Suspensions, Brownian Motion, Molecular Reality: A Short History*, J. Phys. Condens. Matter **14**, 7769 (2002).

[7] D. M. Wilkinson, *Brown Knew Particles Were Smaller than Pollen*, Nature **434**, 137 (2005).

[8] A. Einstein, *Über Die von Der Molekularkinetischen Theorie Der Wärme Geforderte Bewegung von in Ruhenden Flüssigkeiten Suspendierten Teilchen*, Ann. Phys. **322**, 549 (1905).

[9] E. Dickinson, *Food Emulsions and Foams: Stabilization by Particles*, Curr. Opin. Colloid Interface Sci. **15**, 40 (2010).

[10] K. Braun, A. Hanewald, and T. A. Vilgis, *Milk Emulsions: Structure and Stability*, Foods **8**, 1 (2019).

[11] S. H. Lee, R. S. Chadwick, and L. G. Leal, *Motion of a Sphere in the Presence of a Plane Interface. Part 1. An Approximate Solution by Generalization of the Method of Lorentz*, J. Fluid Mech. **93**, 705 (1979).

[12] E. Lauga, M. Brenner, and H. Stone, *Microfluidics: The No-Slip Boundary Condition*, in *Springer Handbook of Experimental Fluid Mechanics*, edited by C. Tropea, A. L. Yarin, and J. F. Foss (Springer Berlin Heidelberg, Berlin, Heidelberg, 2007), pp. 1219–1240.

[13] X. Bian, C. Kim, and G. E. Karniadakis, *111 Years of Brownian Motion*, Soft Matter **12**, 6331 (2016).

[14] Wikimedia Commons contributors, *Biological and Technological Scales Compared*, https://commons.wikimedia.org/w/index.php?title=File:Biological_and_technological_scales_compared-en.svg&oldid=455995727.

[15] M. K. Kim, *Principles and Techniques of Digital Holographic Microscopy*, SPIE Rev. **1**, (2010).

[16] D. Midtvedt, E. Olsén, F. Höök, and G. D. M. Jeffries, *Label-Free Spatio-Temporal*

Monitoring of Cytosolic Mass, Osmolarity, and Volume in Living Cells, Nat. Commun. **10**, (2019).

[17] D. Midtvedt, F. Eklund, E. Olsén, B. Midtvedt, J. Swenson, and F. Höök, *Size and Refractive Index Determination of Subwavelength Particles and Air Bubbles by Holographic Nanoparticle Tracking Analysis*, Anal. Chem. **92**, (2020).

[18] S.-H. Lee, Y. Roichman, G.-R. Yi, S.-H. Kim, S.-M. Yang, A. van Blaaderen, P. van Oostrum, and D. G. Grier, *Characterizing and Tracking Single Colloidal Particles with Video Holographic Microscopy*, Opt. Express **15**, 18275 (2007).

[19] E. van der Pol, L. de Rond, F. A. W. Coumans, E. L. Gool, A. N. Böing, A. Sturk, R. Nieuwland, and T. G. van Leeuwen, *Absolute Sizing and Label-Free Identification of Extracellular Vesicles by Flow Cytometry*, Nanomedicine Nanotechnology, Biol. Med. **14**, 801 (2018).

[20] A. Winters, F. C. Cheong, M. A. Odete, J. Lumer, D. B. Ruffner, K. I. Mishra, D. G. Grier, and L. A. Philips, *Quantitative Differentiation of Protein Aggregates From Other Subvisible Particles in Viscous Mixtures Through Holographic Characterization*, J. Pharm. Sci. **109**, 2405 (2020).

[21] B. Midtvedt, E. Olsén, F. Eklund, F. Höök, C. B. Adiels, G. Volpe, and D. Midtvedt, *Fast and Accurate Nanoparticle Characterization Using Deep-Learning-Enhanced Off-Axis Holography*, ACS Nano **15**, 2240 (2021).

[22] J. Peatross and M. Ware, *Physics of Light and Optics* (Brigham Young University, Department of Physics, 2011).

[23] V. P. Zhdanov, *How the Partial-Slip Boundary Condition Can Influence the Interpretation of the DLS and NTA Data*, J. Biol. Phys. **46**, 169 (2020).

[24] U. C. Boehnke, T. Remmler, H. Motschmann, S. Wurlitzer, and J. Hauwede, *Partial Air Wetting on Solvophobic Surfaces in Polar Liquids*, J. Colloid Interface Sci. **211**, 243 (1999).

[25] J. F. Collis, S. Olcum, D. Chakraborty, S. R. Manalis, and J. E. Sader, *The Measurement of Navier Slip on Individual Nanoparticles in Liquid*, ArXiv (2020).

[26] P. E. Jahl and R. Parthasarathy, *Lipid Bilayer Hydrodynamic Drag*, Phys. Rev. Res. **2**, (2020).

[27] J. Q. Gerlach and M. D. Griffin, *Getting to Know the Extracellular Vesicle Glycome*, Mol. Biosyst. **12**, 1071 (2016).

[28] Y. Yu, M. Li, and Y. Yu, *Tracking Single Molecules in Biomembranes: Is Seeing Always Believing?*, ACS Nano **13**, 10860 (2019).

[29] N. Peerboom, S. Block, N. Altgärde, O. Wahlsten, S. Möller, M. Schnabelrauch, E. Trybala, T. Bergström, and M. Bally, *Binding Kinetics and Lateral Mobility of HSV-1 on End-Grafted Sulfated Glycosaminoglycans*, Biophys. J. **113**, 1223 (2017).

[30] C. F. Bohren and D. R. Huffman, *Absorption and Scattering of Light by Small Particles* (John Wiley & Sons, 2008).

[31] J. D. Jackson, *Classical Electrodynamics* (American Association of Physics Teachers, 1999).

[32] D. K. Cheng and others, *Field and Wave Electromagnetics* (Pearson Education India, 1989).

[33] E. Hecht, *Optics*, fifth edit (Pearson Education Limited, 2017).

[34] J. C. Maxwell, *A Treatise on Electricity and Magnetism*, Vol. 1 (Oxford: Clarendon Press, 1873).

[35] Wikimedia Commons contributors, *Wavelength Slit*, https://commons.wikimedia.org/w/index.php?title=File:Wavelength%3Dslitwidth.gif&oldid=453018513.

[36] R. R. Parwani, *Why Is Schrödinger's Equation Linear?*, Brazilian J. Phys. **35**, 494 (2005).

[37] G. B. Folland, *Fourier Analysis and Its Applications*, Vol. 4 (American Mathematical Soc., 2009).

[38] Y. Cotte, M. F. Toy, E. Shaffer, N. Pavillon, and C. Depeursinge, *Sub-Rayleigh Resolution by Phase Imaging*, Opt. Lett. **35**, 2176 (2010).

[39] J. K. Hannestad, S. Rocha, B. Agnarsson, V. P. Zhdanov, P. Wittung-Stafshede, and F. Höök, *Single-Vesicle Imaging Reveals Lipid-Selective and Stepwise Membrane Disruption by Monomeric a-Synuclein*, Proc. Natl. Acad. Sci. U. S. A. **117**, 14178 (2020).

[40] S. A. Maier, *Plasmonics: Fundamentals and Applications* (Springer Science & Business Media, 2007).

[41] G. Young, N. Hundt, D. Cole, A. Fineberg, J. Andrecka, A. Tyler, A. Olerinyova, A. Ansari, E. G. Marklund, M. P. Collier, and others, *Quantitative Mass Imaging of Single Biological Macromolecules*, Science **360**, 423 (2018).

[42] R. W. Taylor and V. Sandoghdar, *Interferometric Scattering Microscopy: Seeing Single Nanoparticles and Molecules via Rayleigh Scattering*, Nano Lett. **19**, 4827 (2019).

[43] B. Rappaz, P. Marquet, E. Cuche, Y. Emery, C. Depeursinge, and P. J. Magistretti, *Measurement of the Integral Refractive Index and Dynamic Cell Morphometry of Living Cells with Digital Holographic Microscopy*, Opt. Express **13**, 9361 (2005).

[44] J. R. Lakowicz, *Principles of Fluorescence Spectroscopy* (Springer science & business media, 2006).

[45] J. M. Hollas, *Modern Spectroscopy* (John Wiley & Sons, 2004).

[46] Wikimedia Commons contributors, *Jablonski Diagram of Fluorescence Only*, https://commons.wikimedia.org/w/index.php?title=File:Jablonski_Diagram_of_Fluorescence_Only.png&oldid=540353523.

[47] J. Happel and H. Brenner, *Low Reynolds Number Hydrodynamics: With Special Applications to Particulate Media*, (1983).

[48] L. E. Reichl, *A Modern Course in Statistical Physics* (Wiley-VCH, 2017).

[49] R. Kubo, *The Fluctuation-Dissipation Theorem*, Reports Prog. Phys. **29**, 255 (1966).

[50] Wikimedia Commons contributors, *Csm Brownian Motion*,

https://commons.wikimedia.org/w/index.php?title=File:Csm_Brownian-Motion_f99de6516a.png&oldid=490210695.

[51] C. L. Vestergaard, P. C. Blainey, and H. Flyvbjerg, *Optimal Estimation of Diffusion Coefficients from Single-Particle Trajectories*, Phys. Rev. E - Stat. Nonlinear, Soft Matter Phys. **89**, (2014).

[52] M. J. Stephen, *Spectrum of Light Scattered from Charged Macromolecules in Solution*, J. Chem. Phys. **55**, 3866 (1971).

[53] J. L. Anderson, F. Rauh, and A. Morales, *Particle Diffusion as a Function of Concentration and Ionic Strength*, J. Phys. Chem. **82**, 608 (1978).

[54] D. M. Huang, C. Sendner, D. Horinek, R. R. Netz, and L. Bocquet, *Water Slippage versus Contact Angle: A Quasiuniversal Relationship*, Phys. Rev. Lett. **101**, 1 (2008).

[55] I. Fratoddi, *Hydrophobic and Hydrophilic Au and Ag Nanoparticles. Breakthroughs and Perspectives*, Nanomaterials **8**, (2018).

[56] E. Lauga and T. M. Squires, *Brownian Motion near a Partial-Slip Boundary: A Local Probe of the No-Slip Condition*, Phys. Fluids **17**, (2005).

[57] H. Faxén, *Der Gültigkeitsbereich Der Stokes-Oseenschen Wiederstandsformel. Erklärung Einiger von J. Weyssenhoff Gefundener Unstimmigkeiten*, Ann. Phys. **368**, 581 (1920).

[58] H. Faxén, *Der Widerstand Gegen Die Bewegung Einer Starren Kugel in Einer Zähen Flüssigkeit, Die Zwischen Zwei Parallelen Ebenen Wänden Eingeschlossen Ist*, Ann. Phys. **373**, (1922).

[59] A. J. Goldman, R. G. Cox, and H. Brenner, *Slow Viscous Motion of a Sphere Parallel to a Plane Wall-I Motion through a Quiescent Fluid*, Chem. Eng. Sci. **22**, 637 (1967).

[60] H. Brenner, *The Slow Motion of a Sphere through a Viscous Fluid towards a Plane Surface*, Chem. Eng. Sci. **16**, 242 (1961).

[61] S. Leroy, A. Steinberger, C. Cottin-Bizonne, A. M. Trunfio-Sfarghiu, and E. Charlaix, *Probing Biolubrication with a Nanoscale Flow*, Soft Matter **5**, 4997 (2009).

[62] F. Reina, S. Galiani, D. Shrestha, E. Sezgin, G. De Wit, D. Cole, B. Christoffer Lagerholm, P. Kukura, and C. Eggeling, *Complementary Studies of Lipid Membrane Dynamics Using ISCAT and Super-Resolved Fluorescence Correlation Spectroscopy*, J. Phys. D. Appl. Phys. **51**, (2018).

[63] S. Block, B. J. Fast, A. Lundgren, V. P. Zhdanov, and F. Höök, *Two-Dimensional Flow Nanometry of Biological Nanoparticles for Accurate Determination of Their Size and Emission Intensity*, Nat. Commun. **7**, 12956 (2016).

[64] S. Block, V. P. Zhdanov, and F. Höök, *Quantification of Multivalent Interactions by Tracking Single Biological Nanoparticle Mobility on a Lipid Membrane*, Nano Lett. **16**, 4382 (2016).

[65] Y.-H. Liao, C.-H. Lin, C.-Y. Cheng, W. C. Wong, J.-Y. Juo, and C.-L. Hsieh, *Monovalent and Oriented Labeling of Gold Nanoprobes for the High-Resolution Tracking of a Single-Membrane Molecule*, ACS Nano **13**, 10918 (2019).

[66] N. Chenouard, I. Smal, F. De Chaumont, M. Maška, I. F. Sbalzarini, Y. Gong, J.

Cardinale, C. Carthel, S. Coraluppi, M. Winter, A. R. Cohen, W. J. Godinez, K. Rohr, Y. Kalaidzidis, L. Liang, J. Duncan, H. Shen, Y. Xu, K. E. G. Magnusson, J. Jaldén, H. M. Blau, P. Paul-Gilloteaux, P. Roudot, C. Kervrann, F. Waharte, J. Y. Tinevez, S. L. Shorte, J. Willemse, K. Celler, G. P. Van Wezel, H. W. Dan, Y. S. Tsai, C. O. De Solórzano, J. C. Olivo-Marin, and E. Meijering, *Objective Comparison of Particle Tracking Methods*, Nat. Methods **11**, 281 (2014).

[67] A. J. Berglund, *Statistics of Camera-Based Single-Particle Tracking*, Phys. Rev. E - Stat. Nonlinear, Soft Matter Phys. **82**, 1 (2010).

[68] F. Zernike, *Phase Contrast, a New Method for the Microscopic Observation of Transparent Objects*, Physica **9**, 686 (1942).

[69] F. Zernike, *How I Discovered Phase Contrast*, Science **121**, 345 (1955).

[70] T. E. Gureyev and K. A. Nugent, *Rapid Quantitative Phase Imaging Using the Transport of Intensity Equation*, Opt. Commun. **133**, 339 (1997).

[71] Y. Rivenson, Y. Wu, and A. Ozcan, *Deep Learning in Holography and Coherent Imaging*, Light Sci. Appl. **8**, (2019).

[72] I. Yamaguchi and T. Zhang, *Phase-Shifting Digital Holography*, Opt. Lett. **22**, 1268 (1997).

[73] Z. Wang, L. Millet, M. Mir, H. Ding, S. Unarunotai, J. Rogers, M. U. Gillette, and G. Popescu, *Spatial Light Interference Microscopy (SLIM)*, Opt. Express **19**, 2643 (2010).

[74] H. Cao, R. Chriki, S. Bittner, A. A. Friesem, and N. Davidson, *Complex Lasers with Controllable Coherence*, Nat. Rev. Phys. **1**, 156 (2019).

[75] D. Gabor, *A New Microscopic Principle*, Nature **161**, 777 (1948).

[76] E. N. Leith and J. Upatnieks, *Wavefront Reconstruction with Continuous-Tone Objects**, J. Opt. Soc. Am. **53**, 1377 (1963).

[77] M. Hannel, C. Middleton, and D. G. Grier, *Holographic Characterization of Imperfect Colloidal Spheres*, Appl. Phys. Lett. **107**, (2015).

[78] J. B. Sibarita, *Deconvolution Microscopy*, Adv. Biochem. Eng. Biotechnol. **95**, 201 (2005).

[79] L. E. Altman, R. Quddus, F. C. Cheong, and D. G. Grier, *Holographic Characterization and Tracking of Colloidal Dimers in the Effective-Sphere Approximation*, Soft Matter (2021).

[80] G. Zheng, X. Ou, R. Horstmeyer, and C. Yang, *Characterization of Spatially Varying Aberrations for Wide Field-of-View Microscopy*, Opt. Express **21**, 15131 (2013).

[81] J. Fung and S. Hoang, *Computational Assessment of an Effective-Sphere Model for Characterizing Colloidal Fractal Aggregates with Holographic Microscopy*, J. Quant. Spectrosc. Radiat. Transf. **236**, 106591 (2019).

[82] F. Chollet, *Deep Learning with Python* (Manning Publications Co, 2018).

[83] S. Helgadottir, A. Argun, and G. Volpe, *Digital Video Microscopy Enhanced by Deep Learning*, Optica **6**, 506 (2019).

[84] B. Midtvedt, S. Helgadottir, A. Argun, J. Pineda, D. Midtvedt, and G. Volpe,

Quantitative Digital Microscopy with Deep Learning, Appl. Phys. Rev. **8**, 011310 (2021).

[85] Y. Rivenson, T. Liu, Z. Wei, Y. Zhang, K. de Haan, and A. Ozcan, *PhaseStain: The Digital Staining of Label-Free Quantitative Phase Microscopy Images Using Deep Learning*, Light Sci. Appl. **8**, (2019).

[86] L. E. Altman and D. G. Grier, *CATCH: Characterizing and Tracking Colloids Holographically Using Deep Neural Networks*, J. Phys. Chem. B **124**, 1602 (2020).

[87] R. Öz, S. Kk, and F. Westerlund, *A Nanofluidic Device for Real-Time Visualization of DNA-Protein Interactions on the Single DNA Molecule Level*, Nanoscale **11**, 2071 (2019).

[88] S. R. Leslie, A. P. Fields, and A. E. Cohen, *Convex Lens-Induced Confinement for Imaging Single Molecules*, Anal. Chem. **82**, 6224 (2010).

[89] C. Yoshina-Ishii and S. G. Boxer, *Arrays of Mobile Tethered Vesicles on Supported Lipid Bilayers*, J. Am. Chem. Soc. **125**, 3696 (2003).

[90] S. Jõemetsa, P. Joyce, Q. Lubart, M. Mapar, E. Celauro, B. Agnarsson, S. Block, M. Bally, E. K. Esbjörner, G. D. M. Jeffries, and F. Höök, *Independent Size and Fluorescence Emission Determination of Individual Biological Nanoparticles Reveals That Lipophilic Dye Incorporation Does Not Scale with Particle Size*, Langmuir **36**, 9693 (2020).

[91] P. Jönsson, J. P. Beech, J. O. Tegenfeldt, and F. Höök, *Mechanical Behavior of a Supported Lipid Bilayer under External Shear Forces*, Langmuir **25**, 6279 (2009).

[92] M. Bally, A. Gunnarsson, L. Svensson, G. Larson, V. P. Zhdanov, and F. Höök, *Interaction of Single Viruslike Particles with Vesicles Containing Glycosphingolipids*, Phys. Rev. Lett. **107**, 1 (2011).

[93] A. Kunze, M. Bally, F. Höök, and G. Larson, *Equilibrium-Fluctuation-Analysis of Single Liposome Binding Events Reveals How Cholesterol and Ca2+ Modulate Glycosphingolipid Trans-Interactions*, Sci. Rep. **3**, 10 (2013).

[94] P. Joyce, S. Jõemetsa, S. Isaksson, S. Hossain, P. Larsson, C. Bergström, and F. Höök, *TIRF Microscopy-Based Monitoring of Drug Permeation Across a Lipid Membrane Supported on Mesoporous Silica*, Angew. Chemie - Int. Ed. **60**, 2069 (2021).

[95] Wikimedia Commons contributors, *Fluorescence Filters*, https://commons.wikimedia.org/w/index.php?title=File:FluorescenceFilters_2008-09-28.svg&oldid=510174890.

[96] Q. Lubart, J. K. Hannestad, H. Pace, D. Fjällborg, F. Westerlund, E. K. Esbjörner, and M. Bally, *Lipid Vesicle Composition Influences the Incorporation and Fluorescence Properties of the Lipophilic Sulphonated Carbocyanine Dye SP-DiO*, Phys. Chem. Chem. Phys. **22**, 8781 (2020).

[97] E. Van Der Pol, F. A. W. Coumans, A. Sturk, R. Nieuwland, and T. G. Van Leeuwen, *Refractive Index Determination of Nanoparticles in Suspension Using Nanoparticle Tracking Analysis*, Nano Lett. **14**, 6195 (2014).

[98] U. Ortiz-Orruño, A. Jo, H. Lee, N. F. Van Hulst, and M. Liebel, *Precise Nanosizing with High Dynamic Range Holography*, Nano Lett. **21**, 317 (2021).

[99] L. A. Philips, D. B. Ruffner, F. C. Cheong, J. M. Blusewicz, P. Kasimbeg, B. Waisi, J. R. McCutcheon, and D. G. Grier, *Holographic Characterization of Contaminants in Water: Differentiation of Suspended Particles in Heterogeneous Dispersions*, Water Res. **122**, 431 (2017).

[100] A. Einstein, *Physikalische Gesellschaft Zu Berlin Und Deutsche Gesellschaft Für Technische Physik. Berlin, 17. July 1931*, Angew. Chemie **44**, 685 (1931).

[101] J. E. Martin and D. W. Schaefer, *Dynamics of Fractal Colloidal Aggregates*, Phys. Rev. Lett. **53**, 2457 (1984).

[102] S. Zhang, H. Gao, and G. Bao, *Physical Principles of Nanoparticle Cellular Endocytosis*, ACS Nano **9**, 8655 (2015).

[103] G. Emilsson, R. L. Schoch, L. Feuz, F. Höök, R. Y. H. Lim, and A. B. Dahlin, *Strongly Stretched Protein Resistant Poly(Ethylene Glycol) Brushes Prepared by Grafting-To*, ACS Appl. Mater. Interfaces **7**, 7505 (2015).

[104] K. Goto and Y. Hayasaki, *Three-Dimensional Motion Detection of a 20-Nm Gold Nanoparticle Using Twilight-Field Digital Holography with Coherence Regulation*, Opt. Lett. **40**, 3344 (2015).

[105] P. Kukura, A. Weigel, and J. Benesch, *Interferometric Scattering Microscopy*, US 10,775,597 B2 (2020).

[106] C. Y. Cheng, Y. H. Liao, and C. L. Hsieh, *High-Speed Imaging and Tracking of Very Small Single Nanoparticles by Contrast Enhanced Microscopy*, Nanoscale **11**, 568 (2019).

[107] M. Wallert, C. Nie, P. Anilkumar, S. Abbina, S. Bhatia, K. Ludwig, J. N. Kizhakkedathu, R. Haag, and S. Block, *Mucin-Inspired, High Molecular Weight Virus Binding Inhibitors Show Biphasic Binding Behavior to Influenza A Viruses*, Small **16**, 1 (2020).

[108] S. Alberti, A. Gladfelter, and T. Mittag, *Considerations and Challenges in Studying Liquid-Liquid Phase Separation and Biomolecular Condensates*, Cell **176**, 419 (2019).